The Astrophysical Journal, 825:1 (22pp), 2016 July 1 doi:10.3847/0004-637X/825/1/1

SHOCK CONNECTIVITY IN THE 2010 AUGUST AND 2012 JULY SOLAR ENERGETIC PARTICLE EVENTS INFERRED FROM OBSERVATIONS AND ENLIL MODELING

H. M. Bain[1], M. L. Mays[2,3], J. G. Luhmann[1], Y. Li[1], L. K. Jian[3,4], and D. Odstrcil[3,5]
[1] Space Sciences Laboratory, UC Berkeley, 7 Gauss Way, Berkeley, CA 94720-7450, USA; hbain@ssl.berkeley.edu
[2] Catholic University of America, Washington, DC, USA
[3] Heliophysics Science Division, NASA Goddard Space Flight Center, Greenbelt, MD 20771, USA
[4] University of Maryland, College Park, MD 20742, USA
[5] George Mason University, Fairfax, VA, USA
Received 2015 September 12; accepted 2016 April 15; published 2016 June 24

ABSTRACT

During periods of increased solar activity, coronal mass ejections (CMEs) can occur in close succession and proximity to one another. This can lead to the interaction and merger of CME ejecta as they propagate in the heliosphere. The particles accelerated in these shocks can result in complex solar energetic particle (SEP) events, as observing spacecraft form both remote and local shock connections. It can be challenging to understand these complex SEP events from in situ profiles alone. Multipoint observations of CMEs in the near-Sun environment, from the *Solar Terrestrial Relations Observatory*–Sun Earth Connection Coronal and Heliospheric Investigation and the *Solar and Heliospheric Observatory* Large Angle and Spectrometric Coronagraph, greatly improve our chances of identifying the origin of these accelerated particles. However, contextual information on conditions in the heliosphere, including the background solar wind conditions and shock structures, is essential for understanding SEP properties well enough to forecast their characteristics. Wang–Sheeley–Arge WSA-ENLIL + Cone modeling provides a tool to interpret major SEP event periods in the context of a realistic heliospheric model and to determine how much of what is observed in large SEP events depends on nonlocal magnetic connections to shock sources. We discuss observations of the SEP-rich periods of 2010 August and 2012 July in conjunction with ENLIL modeling. We find that much SEP activity can only be understood in the light of such models, and in particular from knowing about both remote and local shock source connections. These results must be folded into the investigations of the physics underlying the longitudinal extent of SEP events, and the source connection versus diffusion pictures of interpretations of SEP events.

Key words: Sun: activity – Sun: coronal mass ejections (CMEs) – Sun: heliosphere

1. INTRODUCTION

Sufficiently fast coronal mass ejections (CMEs) and their interplanetary counterparts (ICMEs) are capable of driving collisionless shocks in the corona and interplanetary medium that can accelerate particles to high energies. These so-called solar energetic particle (SEP) events include ion populations, primarily protons, with energies in the range of tens of keV to a few GeV, lasting for hours to several days. Many factors contribute to the time–intensity profile of an SEP. Where it was once considered that impulsive SEP events were flare-associated and gradual events were related to interplanetary shocks, Cane et al. (2010) more recently found there to be a continuum of event characteristics. The study found no specific solar parameter, such as flare or CME associations, to distinguish between five groups of events, which were defined based on particle abundances and event profiles. However, there was a distinction between SEP events with associated type III radio bursts, the relative timing of which was indicative of the manner in which particles were accelerated and/or released, and was reflected in the composition of the SEP. Type III bursts occurring during the impulsive phase of the flare were typically associated with electron-rich proton events of lower intensity and short duration. SEP events where the type III bursts occurred after the impulsive phase were found to be associated with the larger events.

The longitudinal position of the observer with respect to the source region of the CME parent, and the observer's magnetic connectivity to the shock, contribute greatly to the timing and intensity profiles of each SEP event (Cane et al. 1988, 2010; Reames 1999). The shock is often fastest and strongest near the central region (nose), producing the strongest acceleration, while the speed and strength of the shock are expected to decline along the flanks. Assuming parallel (to the magnetic field) transport dominates, the shock properties at a particular observer's magnetic connection point should determine the intensity and energy spectrum of the detected SEP event as the shock and connection point evolve with time. This general picture, which emphasizes the role of the evolution of the shock source and the magnetic connection point, has been applied with some success to the study of observed events by, e.g., Kallenrode & Wibberenz (1997) and Lario et al. (2013).

One of the major challenges of this type of interpretation has been the availability of realistic descriptions of the heliosphere and the evolution of the shock source during the SEP events under study. As a general rule, for an Earth-based observer, SEP events associated with CMEs originating on the west limb of the Sun typically exhibit a prompt onset and relatively rapid decay, as the observer is initially well connected to the shock in the corona but then loses that connection as the shock moves outward. For events originating on the east limb, the SEP profile exhibits a gradual onset as the observer becomes connected to the shock as it moves outward, away from the Sun and beyond the observer's radial location. The SEP profile for a shock headed toward the observer typically peaks in intensity as the shock reaches the observer in such events, producing an enhancement due to the energetic solar particle event (ESP) on

the gradual SEP event profile. The ESP-enhanced fluxes often exhibit a softer spectrum than that in the underlying event.

In addition to the observer's magnetic connection to the shock, the heliospheric conditions in which the shock is propagating can significantly affect the SEP timing and intensity profile. For example, during active periods there can be multiple, closely timed and closely spaced CMEs driving shocks through the heliosphere, which can merge and produce complex SEPs over a wide range in longitude. In some cases the observer may also be magnetically connected to the shock (s) from behind, while in other cases particles may be observed as a result of magnetic mirroring or from a reflecting boundary (e.g., a stream interaction region (SIR)) beyond the observer. SEPs can also be magnetically trapped between two field maxima from SIRs or CME shock/sheaths along the observer's field lines. These complex events can be difficult to interpret from inspection of in situ observations alone.

Multi-perspective CME information from the *Solar Terrestrial Relations Observatory*–Sun Earth Connection Coronal and Heliospheric Investigation (*STEREO*-SECCHI: Howard et al. 2008) suite of instruments and the *Solar and Heliospheric Observatory* (*SOHO*: Domingo et al. 1995) Large Angle and Spectrometric Coronagraph (LASCO: Brueckner et al. 1995), together with the spatially separated multipoint in situ measurements from the *Advanced Composition Explorer* (*ACE*: Stone et al. 1998) and *STEREO* (Luhmann et al. 2008) at 1 AU have significantly improved our ability to perform diagnostics of real SEP events. In particular, the empirical paradigm describing the spatial dependence of the time profiles proposed decades ago by Cane et al. (1988, 2010) has become more testable. One key uncertainty of their picture continues to be the extent to which perpendicular transport of particles (by diffusion and/or drifts) across the magnetic field determines what is observed, as opposed to temporal and spatial evolution of the moving shock to which the observer is magnetically connected (and parallel propagation dominates) (e.g., see Kallenrode & Wibberenz 1997; Lario et al. 1998; Luhmann et al. 2010). The aim of the present study is to test to what extent SEP observations can be described by the latter. In other words, can the observer's magnetic connection to the moving, evolving shock source explain most of what is observed?

To determine whether SEP events at a given location can be understood from the paradigm of the observer's connection to the source requires a realistic picture of the global background solar wind through which the shocks and SEPs propagate. Computational models such as the Wang–Sheeley–Arge WSA-ENLIL + Cone model (Odstrčil et al. 1996; Arge & Pizzo 2000; Odstrcil 2003; Arge et al. 2004) provide such a tool. In addition to giving contextual information on background solar wind structures (i.e., CMEs and SIRs), such models allow explicit determination of the observer's magnetic connectivity to the shock and the source region, including contributing factors in that connectivity such as prior CME events, as well as the connected shock properties (e.g., speed, angular width, shock strength, etc.).

In this paper we discuss the SEP events occurring in the months of 2010 August and 2012 July. These periods occurred at times of increased solar activity in the rising phase of solar cycle 24, resulting in multiple CME-driven shocks and multiple SEP events. While it is clear that there are many factors that can define the time–intensity profile, we explore ways in which the shock connectivity, inferred from *SOHO* and *STEREO* coronagraph-based WSA-ENLIL + Cone models, of several weeks duration, contributes to the observed characteristics of the SEP events. Using the measurements from *STEREO* and *ACE*, we examine SEP proton time profiles present in these events and discuss their attributes in the context of the spacecraft's magnetic connectivity to the shock and the state of the surrounding heliosphere. In addition to testing the explanation for SEP profile characteristics in terms of shock connection, this study shows how WSA-ENLIL + Cone models can be used for both diagnostics of SEP events as well as potential forecasting of them. In Section 2 we introduce the WSA-ENLIL + Cone model. In Sections 3 and 4 we discuss the 2010 August and 2012 July periods, respectively, and in Section 5 we discuss our findings.

2. WSA-ENLIL + CONE MODEL

The WSA-ENLIL + Cone model provides a tool for investigating connectivity between observer and shock as a function of time for real case studies such as the 2010 August and 2012 July SEP events. The global 3D MHD WSA-ENLIL model (Arge et al. 2004; Odstrcil et al. 2004) uses synoptic solar magnetic field maps derived from magnetograms as a basis for a time-dependent, background heliospheric description outside of 21.5 $R_\odot$, into which spherical shaped high-pressure gusts are injected to emulate observed CME-related solar wind disturbances. ENLIL-modeled CMEs do not contain internal magnetic structures and are instead hydrodynamic disturbances with unchanged background magnetic field. The WSA-ENLIL + Cone modeling is arguably one of the most realistic simulations of interplanetary conditions, including ICME shocks, available for real-time modeling. The model system does not simulate the CME initiation but uses kinematic properties of CMEs, inferred from coronagraphs, to launch a CME-like hydrodynamic structure into the solar wind and interplanetary magnetic field computed from the WSA coronal model (Arge & Pizzo 2000; Arge et al. 2004). In this work the graduated cylindrical shell (GCS) model (Thernisien et al. 2009) was used to fit the 3D propagation of the CME using multipoint WL coronagraph observations from *STEREO A/B* and LASCO. WSA-ENLIL + Cone runs performed for research and operations have shown that accurate descriptions of the heliosphere are achieved only when the background solar wind is well reproduced and if multipoint coronagraph observations are used to derive CME parameters (Lee et al. 2013; Mays et al. 2015).

For the 2010 August and 2012 July case studies discussed in this paper, we model extended event periods of 26 and 20 days respectively, choosing to inject only the fast CMEs ($v > 500$ km s^{-1} at the Sun) that likely drove a coronal or interplanetary shock, accelerating particles that contributed to the observed SEP events. Throughout the model run, we track the simulated CME propagation from the ENLIL inner boundary of 21.5 $R_\odot$ out to 5.3 AU. The chosen distance of the outer boundary allows for the most significant magnetic reflections from magnetic compressions due to solar wind SIRs or prior CME events. These simulations were performed on a low-resolution (4°) spherical grid of size 832 × 30 × 90 (r, θ, ϕ) with an output cadence of five to ten minutes at locations of interest, and a full three-dimensional output cadence of one hour. The simulation range is 0.1–5.5 AU in radius [r], −60° to +60° in latitude [θ], and 0°–360° in longitude [ϕ]. For the purposes of this study, one background

(ambient) solar wind simulation was performed along with simulations for each CME, including any prior CMEs. For example, for a period with three CMEs of interest, four simulations were performed with the same inner boundary and numerical conditions. The four simulations would consist of: no CMEs (background), CME1, CME1 + CME2, CME1 + CME2 + CME3. This allows one to subtract the previous simulation and obtain and track the contributions from each CME shock front separately, while still allowing the CMEs to interact during propagation. For each subtracted simulation, shocks are identified as increases of more than 20 km s^{-1} (compared to the ambient simulation) along magnetic field lines connected to the observer starting at the outer boundary of 5.5 AU. This scheme allows us to identify both remote and local magnetic connections to the shock from the *STEREO A* and *B* spacecraft, and at Earth at, e.g., *ACE*. The ENLIL model returns information regarding the simulated shock parameters, such as shock position, velocity, angle between the shock normal and the ambient magnetic field (θ_{BN}), and solar wind parameters such as density and velocity both up- and downstream of the shock, along observer-connected magnetic field lines. This information alone is valuable for studies of SEP events in that it allows remote sensing of shocks that cannot otherwise be obtained from either imaging or in situ measurements.

3. 2010 AUGUST EVENTS

The period from the end of 2010 July and throughout August was characterized by increased solar activity. Figure 1 shows an overview of the period. The top and bottom rows show time profiles of proton intensity from the *STEREO A* and *B* Low and High Energy Telescopes (LET: Mewaldt et al. 2008; HET: von Rosenvinge et al. 2008) from 2010 July 31 to August 27. The middle panel shows proton intensities at Earth from the Electron, Proton and Alpha Monitor (EPAM) instrument on board *ACE*. Vertical solid black lines and orange shaded regions indicate observed shock arrivals and magnetic cloud (MC) passages at the spacecraft, respectively, as identified by in situ solar wind and magnetic field parameters from the Plasma and Suprathermal Ion Composition instrument (PLASTIC: Galvin et al. 2008) and the Magnetic Field Experiment instrument (MAG: Acuña et al. 2008) on board *STEREO* and the Solar Wind Electron Proton Alpha Monitor (McComas et al. 1998) and the Magnetic Fields Experiment (MAG: Smith et al. 1998) instruments on board *ACE*. In particular, we have used the publicly available *STEREO* shock list compiled by Lan Jian (http://www-ssc.igpp.ucla.edu/forms/stereo/stereo_level_3.html) (Jian et al. 2013) and the online database of interplanetary shocks observed by *ACE*, compiled by the Harvard–Smithsonian Center for Astrophysics (http://www.cfa.harvard.edu/shocks/ac_master_data/). Shocks are numbered in accordance with the numbering of their CME driver, Table 1. Green and red vertical dashed lines are related to the modeling, indicating ENLIL predictions for the time that the spacecraft first becomes magnetically connected to the shock and the predicted shock arrival at the spacecraft, respectively. Numbering of the ENLIL shock connectivity corresponds to the CME numbering defined in Table 1. The time at which ENLIL predicts that the spacecraft becomes magnetically connected to the shock (green vertical lines) can occur when the shock is at any distance within the simulation domain, e.g., inside 1 AU or beyond the spacecraft depending on the situation. The ENLIL results, and their relation to the observed shocks, are discussed in more detail in the following sections.

An overview of the SEP events (labeled AUGSEP1–AUGSEP4) and their associated CME(s) (labeled CME1–CME6) is detailed in Table 1. CME start times and velocities labeled with † indicate values taken from detailed studies of the CME propagation already available in the literature (references for which are mentioned explicitly in the following sections). Values reported from the literature are not taken at 21.5 $R_\odot$ and can therefore be quite different in magnitude from those used as an input to ENLIL, but are reported here to make clear which CMEs are used in this study in reference to previous work. CMEs labeled with * indicate values taken from the LASCO CME catalog, where the start time is taken as the first appearance of the CME leading edge in the LASCO C2 field of view and the speed is a second-order fit value taken at 20 $R_\odot$ from LASCO plane-of-sky measurements. Start times and velocities shown in brackets and source origin (latitude and longitude) are those used as an input to the ENLIL modeling at 21.5 $R_\odot$, determined from 3D reconstructions of the CME front. Also listed are the observed shock arrival times at each spacecraft, corresponding to those marked in Figure 1, which are labeled S1-6 in accordance with the corresponding CME numbering.

Figure 2 shows a series of snapshots of radial velocity contours (cropped to 2 AU from a 5.5 AU run for clarity) taken throughout a 26 day ENLIL model run beginning on 2010 July 30. The input synoptic map from the WSA model for this period was computed from a single magnetogram from the National Solar Observatory *Global Oscillation Network Group* (GONG: Harvey et al. 1996) for Carrington rotation 2100 and Carrington longitude 348° on 2010 August 5 at 23:54 UT, which was rotated backwards to the start of the simulation period. Small latitudinal shifts in the magnetogram-derived coronal maps caused by inaccuracies in observations of solar magnetic field can cause large longitudinal shifts at 1 AU, for example in characterizing high-speed stream arrival times (e.g., MacNeice 2009; Jian et al. 2011, 2015). This later magnetogram was chosen for this event period because the evolution of active regions on the far side of the Sun could not be captured by earlier magnetograms (Schrijver & Title 2011). Injected into the WSA background solar wind, at the 21.5 $R_\odot$ ENLIL inner boundary, are the spherical approximations of six CMEs, with properties listed in Table 1. The default ENLIL CME density ratio factor (dcld) of 4 was used for all CMEs except CME3, for which dcld = 6 was used supported by the CME brightness in the coronagraph observations. The default factor of dcld = 4 has worked well for typical CMEs, and together with the CME width it determines the CME mass. ENLIL is more sensitive to the CME input speed than to other CME parameters. Taktakishvili et al. (2010) showed that for three Earth-directed CME events of varying speed, the modeled CME arrival varied by 2–6 hr (depending on the event) when the density ratio was adjusted from 2 to 4. Mays et al. (2015) showed that for one event the arrival time varied by up to 4 hr when the density ratio was adjusted from 4 to 2. The right-hand panel of Figure 2 shows temporal profiles of the observed (red) and simulated (blue) radial solar wind velocity at Earth, *STEREO A*, *STEREO B*, and Mars.

At intervals of five minutes throughout the simulation, we located the connections via magnetic field lines of each observer (*ACE*, *STEREO A*/*B*) to the shocks produced by all

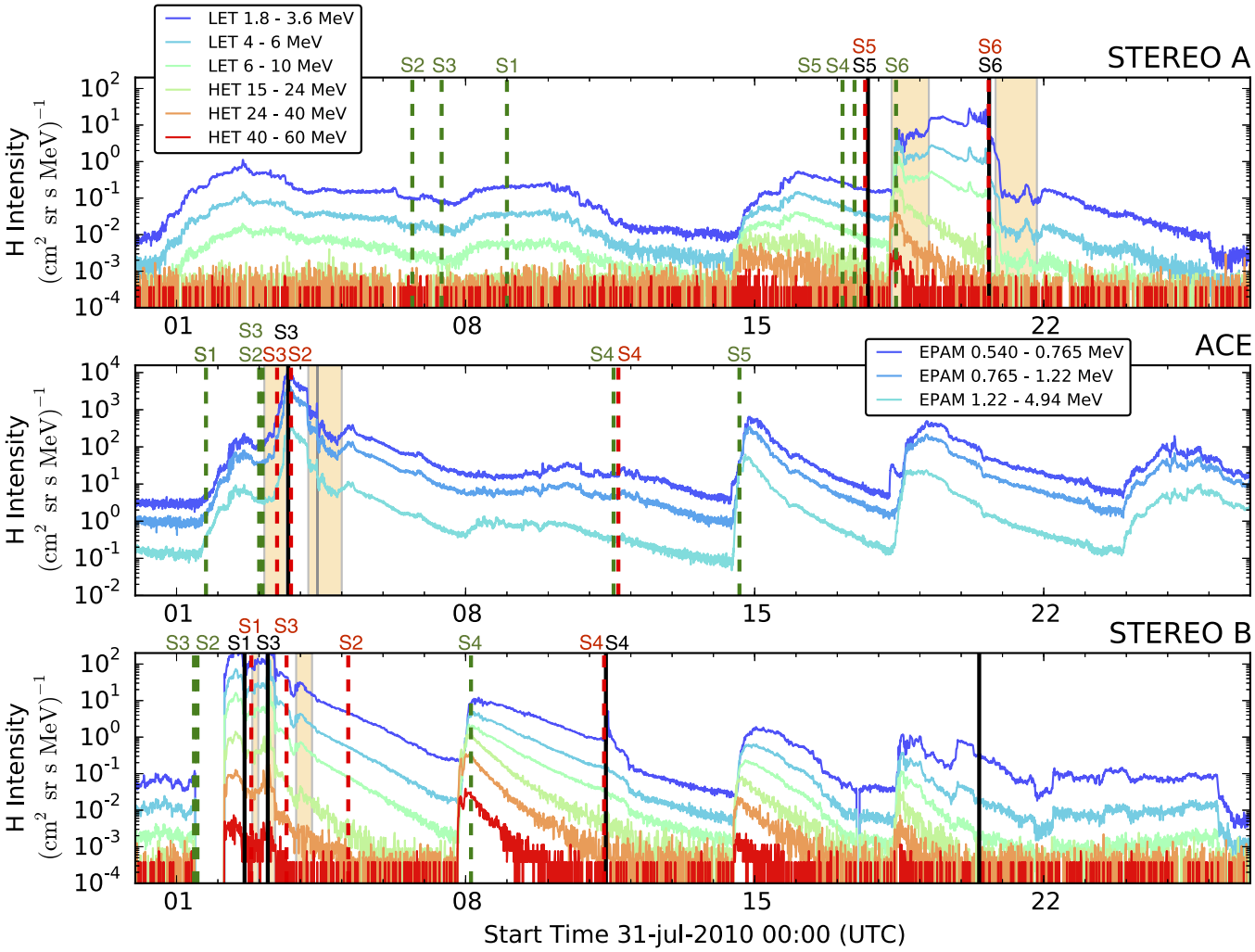

Figure 1. Proton time profiles from the *STEREO* LET and HET (*STEREO A*: top and *STEREO B*: bottom) and *ACE* EPAM (middle) instruments for the 2010 August period of SEP events. Black vertical solid lines indicate shock arrivals at the spacecraft, numbered to reference the CME numbers defined in Table 1. Orange shaded time periods indicate magnetic cloud passages observed at the spacecraft. Green vertical dashed lines indicate the times when the spacecraft first becomes magnetically connected to the shock as simulated by ENLIL modeling. Red vertical lines indicate the ENLIL-predicted shock arrival time at each spacecraft. ENLL shock connections are also numbered with reference to the CME numbers defined in Table 1.

CMEs. For times when the spacecraft were connected to a shock, Figure 3 (top row), the simulation returns information on the shock and solar wind properties at the shock on the spacecraft-connected field line. Figure 3 row 2 shows the shock velocity $v_{\rm shock}$; row 3 shows the ratio of the solar wind density upstream to downstream of the shock (n_1/n_0); row 4 shows the ratio of the solar wind velocity upstream to downstream of the shock (v_1/v_0); and row 5 shows $\theta_{\rm BN}$, the angle between the shock normal and the upstream interplanetary magnetic field. Of particular interest are the times at which each spacecraft becomes magnetically connected to the shock, the arrival time, and the shock parameters at each spacecraft for comparison with in situ measurements. The results of the simulation are compared with observations in Tables 2 and 3. In the following sections we concentrate on the complex case-study events of AUGSEP1 and AUGSEP4. This comparison provides an assessment of the extent to which observer connections to CME-produced shocks, together with the evolving shock parameters, explain what is observed in the SEP time profile.

3.1. AUGSEP1: August 1 07:00 UT to August 7 12:00 UT

The first SEP event in the 2010 August series (AUGSEP1) is complex, consisting of two shocks and three magnetic flux ropes from three interacting CMEs. Figure 4 shows an overview of the plasma and magnetic field parameters from *STEREO B* (top) and *ACE* (bottom). The CMEs associated with AUGSEP1 did not propagate in the direction of *STEREO A* or produce a significant SEP event at that spacecraft. The top rows of both panels in Figure 4 show time profiles of proton intensity: 1.8–60 MeV protons from *STEREO B* LET and HET (top panel, row 1) and EPAM 0.540–4.94 MeV from *ACE* (bottom panel, row 1). Rows 2 and 3 show magnetic field components ($B_{x,y,z}$ from *ACE* and $B_{\rm R,T,N}$ from *STEREO B*) and total magnitude, $|B|$, respectively. Rows 4–6 show the solar wind speed, v, proton density, n_p, and temperature, T.

For *STEREO B*, rows 7 and 8 show 4–6 MeV proton intensities from the LET instrument. The LET instrument measures particle flows as a function of viewing angle with respect to the Sun by observing proton intensities from two

Table 1
2010 August SEP Events

SEP	Start Time (UT)	End Time (UT)	CME					Shock Arrival		
			No.	Start Time (UT)	Velocity (km s^{-1})	Lat. (deg)	Long. (deg)	*STB* (UT)	Earth (UT)	*STA* (UT)
AUGSEP1	Aug 1 07:00	Aug 7 12:00	CME1	Jul 30 07:30† (16:08)	540† (750)	12	−68	Aug 2 15:31	⋯	⋯
			CME2	Aug 1 02:42† (08:10)	730† (760)	7	−22	⋯	⋯	⋯
			CME3	Aug 1 07:48† (11:20)	1140† (1300)	18	−48	Aug 3 05:00	Aug 3 16:54	⋯
AUGSEP2	Aug 7 00:00	Aug 14 12:00	CME4	Aug 7 18:36* (23:15)	827* (750)	−3	-46	Aug 11 9:31	⋯	⋯
AUGSEP3	Aug 14 12:00	Aug 17 20:50	CME5	Aug 14 10:12* (14:00)	989* (950)	−7	46	⋯	⋯	Aug 17 17:50
AUGSEP4	Aug 17 21:00	Aug 21 08:20	CME6	Aug 18 05:48* (08:40)	1416* (1250)	−6	42	⋯	⋯	Aug 20 16:13

Note. Column 1 labels each SEP event in the August series, with start and end times defined in columns 2 and 3. Columns 4–8 contain information on the CME(s) associated with each SEP event. Column 4: CME label. Column 5: CME start time (events marked † indicate CME start times taken from the literature and explicitly mentioned in the text below, ∗ indicate start times taken from the LASCO CME catalog http://cdaw.gsfc.nasa.gov/CME_list/, when the CME leading edge first appears in the C2 field of view), and in brackets the time that the CME enters the ENLIL simulation at 21.5 $R_{\odot}$. Column 6: CME initial velocity (events marked † indicate CME initial velocities taken from the literature, * indicate the second-order speed at 20 $R_{\odot}$, from plane-of-sky measurements of the CME, taken from the LASCO CME catalog), in brackets is the CME velocity at 21.5$R_{\odot}$ used as an input to the ENLIL modeling, determined using 3D reconstructions of the CME front from multipoint white-light (WL) coronagraph observations. Columns 7 and 8: latitude and longitude of CME origin. Columns 9–11 list shock arrival times at *STEREO B* (*STB*), Earth, and *STEREO A* (*STA*).

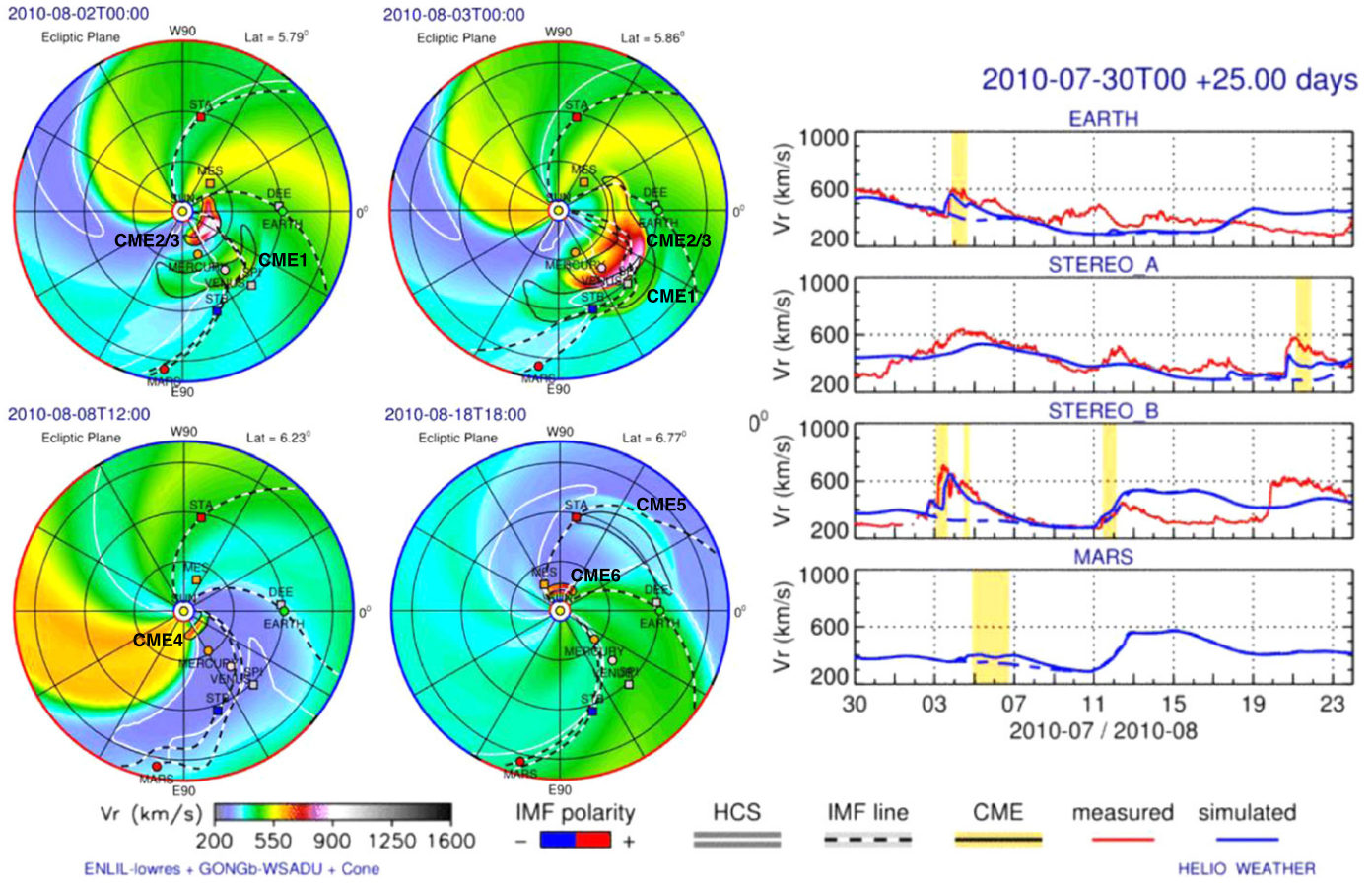

Figure 2. Left: radial velocity contour plots at four times during the ENLIL 2010 August simulation run, cropped to 2 AU. Black and white dashed lines show the simulated magnetic connectivity of each spacecraft to structures in the heliosphere. Right: profiles of the observed (red) and simulated (blue) radial solar wind velocity at Earth, *STEREO A*, *STEREO B*, and Mars.

fans covering 16 different viewing angles spanning 133° in longitude (Figure 5) and $\pm 15° - 20°$ elevation out of the ecliptic (Mewaldt et al. 2008). The two fans are centered on the nominal Parker spiral in the Sun and anti-Sun directions, providing both time profiles of the proton flux for each energy channel and diagnostics of particle flows "toward" and "away" from the Sun, along the Parker spiral. Together with magnetic field measurements from MAG, particle pitch angle distributions, indicating the particle motion with respect to the magnetic field, are observed. However, because of the near-ecliptic nature of these measurements, these are only 2D distributions, and cannot be reconstructed when the interplanetary field has a high inclination. In many cases the history of pitch angle distribution for an individual event can be complex (Leske et al. 2012), with periods of unidirectional streaming, bidirectional streaming, and isotropic distributions appearing at different times in relation to their association with the ICME shock and MC structures (Richardson & Reames 1993; Leske et al. 2012, 2013). In Figure 4 rows 7 and 8 of the *STEREO B* panel show 4–6 MeV proton intensities from the 16 LET detector sectors, shown first as an intensity profile and then as a spectrogram. The line colors used for the time profile in row 7 correspond to the LET viewing angle with respect to the Sun, see Figure 5 for reference. Overplotted gray and black profiles in row 8 represent the radial–tangential–normal (RTN) longitude of the magnetic field ($B_{\rm long} = \tan^{-1}(B_{\rm T}/B_{\rm R})$). Combining information regarding the direction of proton flow from the sectored LET data with knowledge of the magnetic field direction, row 9 shows the resulting pitch angle distribution, $\cos(\phi)$. Black vertical solid lines denote shocks observed in situ. Green and red vertical dashed lines denote the timing of remote and local shock connections from ENLIL simulations. This is discussed in more detail in the following sections.

Shock 1 (S1), identified in *STEREO B* at 15:30 UT on August 2, is associated with CME1, which left the Sun around 07:30 UT on July 30 with a velocity of 540 km s^{-1} (Liu et al. 2012). The arrival of the associated magnetic structure M1 is highlighted by an orange shaded band. Shock 3 (S3), observed by *STEREO B* at 05:00 UT on August 3 and later at 16:54 UT on August 3 at *ACE*, is the result of a CME–CME interaction. On 2010 August 1, a series of four CMEs were observed propagating in the longitudinal range 25° east to 8° west of the Sun–Earth line (Möstl et al. 2012). Two of these events, CME2 and CME3, left the Sun within a short timeframe, at 02:42 UT and 07:48 UT, with speeds of 730 and 1140 km s^{-1}, respectively (Liu et al. 2012). CME2 and CME3 were observed to interact around 55 $R_\odot$, as the second, faster CME caught up with the first, slower moving event (Liu et al. 2012; Martínez Oliveros et al. 2012; Temmer et al. 2012). From an investigation of remote observations and in situ measurements, Liu et al. (2012) found that, following the interaction of CME2 and CME3, the merged structure continued to propagate as a single entity while the magnetic structure of each event remained identifiable (M3), with the ejecta from CME2 being compressed by CME3. The shock, labeled S3 to highlight the

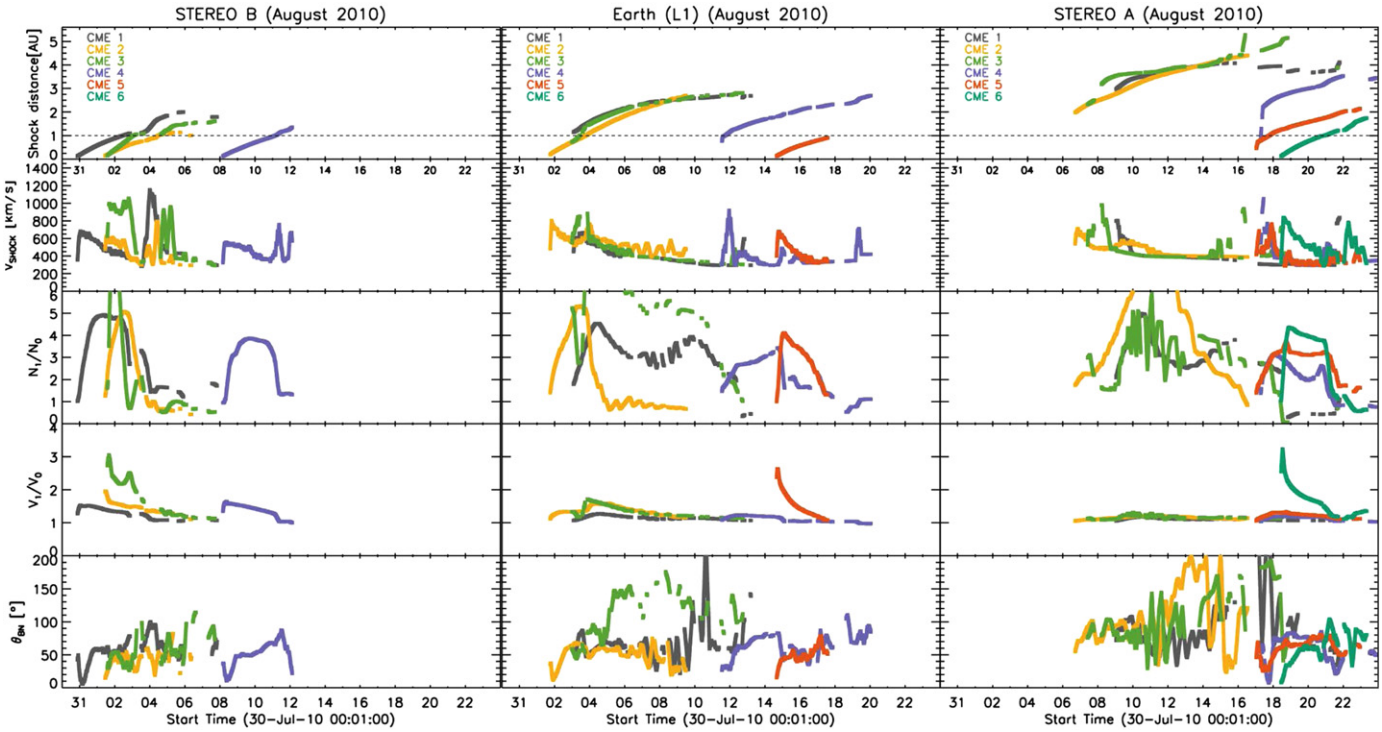

Figure 3. From ENLIL modeling of the 2010 August periods, the top row of each plot shows periods when *STEREO B* (left), Earth/*ACE* (middle), and *STEREO A* (right) were connected to shocks associated with CMEs 1–6 and the shock distance from the Sun at that time. Rows 2–5 show the shock and solar wind properties at the shock on the spacecraft-connected field line: the shock velocity (row 2); the ratio of the solar wind density upstream and downstream of the shock, n_1/n_0 (row 3); the ratio of the solar wind velocity upstream and downstream of the shock, v_1/v_0 (row 4); and θ_{BN}, the angle between the shock normal and the interplanetary magnetic field.

fact that CME3 merged with CME2, comprised the newly formed front. Further to the interaction of CME2 and CME3 at 55 $R_\odot$, remote observations and in situ measurements suggest that S3 is propagating through the ejecta from CME1 as it passes *STEREO B* (Liu et al. 2012; Möstl et al. 2012). The authors interpret M2 as the shocked portion of M1, as S3 passes through it. Möstl et al. (2012) found S3 to be quasi-perpendicular at *STEREO B*. This supports the finding that shocks are more likely to be quasi-perpendicular when traveling inside an ICME (Richardson & Cane 2010; Lugaz et al. 2015).

Figure 6 shows the arrival of both shocks at *STEREO B* more closely. At 10:00 UT, 5 hr prior to S1, LET detects an increase in protons flowing away from the Sun. For well-connected events, field-aligned unidirectional proton flows are often observed streaming away from the shock, toward the observer several hours ahead of the shock's arrival (Leske et al. 2013). These particles are initially accelerated in the shock before escaping onto observer-connected field lines. As the spacecraft connectivity with the shock changes, these unidirectional particle flows can appear intermittent. Figure 6 shows particle flows away from the Sun prior to S1. Around 04:00 UT, in the hour leading up to the arrival of S3, LET observed particle flows separated by $\sim 180^\circ$, which are initially aligned with the magnetic field direction and then drift to flows perpendicular to the magnetic field direction. Bidirectional flows have been observed to be associated with the MC part of an ICME, though there is not an exact matching of the times of bidirectional flows and the MC boundaries (Richardson & Reames 1993; Richardson 1994). However, typically these counter-streaming flows are aligned with the magnetic field direction. In event 1, the flow direction moves away from field alignment.

The top two contour plots of radial velocity in Figure 2 at 00:00 UT on August 2 and 00:00 UT on August 3 correspond to the CME events of AUGSEP1. At 00:00 UT on August 2 ENLIL shows CME1 shortly before it reaches *STEREO B*, followed by the merged structure of CME2 and CME3. By 00:00 UT on August 3, the merged structure of CME2 and CME3 has caught up with the rear of CME1 as it passes *STEREO B*, as expected. The ENLIL modeling results support the results of previous studies in the literature mentioned above, in terms of the propagation. Another positive result of the modeling is the time that the model predicts at which *ACE* and *STEREO B* first become magnetically connected to shocks S1, S2, and S3; see the green dashed vertical lines in Figure 4. At both of these spacecraft the first connection to the shock occurs within a few hours of the time at which the proton intensity profiles show an increase. Although particles accelerated in shocks 1–3 do not result in a significant SEP at *STEREO A*, ENLIL modeling does show a remote connection to shocks from all three CMEs several days later when the shocks are beyond 2 AU; see Figures 1 and 3 (top right).

However, Figure 4 shows the simulated shock arrival time (red dashed vertical lines) for S1 and S3 occurring several hours after the observed shocks (black solid vertical lines) at *STEREO B*, and S3 occurring several hours earlier than observed at *ACE* (see also Table 2). Furthermore the model finds a "false alarm" shock passage of S2 at both *STEREO B* and *ACE*, but it is possible that *STEREO B* missed the shock due to a data gap. As can be seen in Figure 3 (top left), S3

Table 2
2010 August ENLIL Shock Connectivity Results

	First Shock Connection			Shock Arrival					
	STB UT (AU)	Earth UT (AU)	*STA* UT (AU)	*STB* (UT)		Earth (UT)		*STA* (UT)	
				Obs.	**Sim.**	Obs.	**Sim.**	Obs.	**Sim.**
S1	Jul 30 20:09 (0.12)	Aug 3 2:00 (0.15)	Aug 9 00:01 (2.94)	Aug 2 15:30	**Aug 2 19:26**	…	…	…	…
S2	Aug 1 10:07 (0.13)	Aug 1 17:06 (0.17)	Aug 6 17:00 (1.98)		(**Aug 5 3:46**)		(**Aug 3 18:31**)	…	…
S3	Aug 1 12:09 (0.11)	Aug 3 00:00 (0.74)	Aug 7 10:03 (2.33)	Aug 3 05:00	**Aug 3 15:55**	Aug 3 16:54	**Aug 3 10:25**	…	…
S4	Aug 8 3:07 (0.12)	Aug 11 14:00 (0.95)	Aug 17 10:01 (2.20)	Aug 11 9:31	**Aug 11 8:27**	…	**Aug 11 16:46**	…	…
S5	…	Aug 14 14:00 (0.12)	Aug 17 03:02 (0.73)	…	…	…	…	Aug 17 17:50	**Aug 17 16:10**
S6	…	…	Aug 18 10:09 (0.11)	…	…	…	…	Aug 20 16:13	**Aug 20 15:58**

Note. Left columns list the time when each spacecraft first becomes magnetically connected to each shock, and at what radial distance, for CMEs 1–6. Right columns show the observed shock arrival times and the predicted arrival times from the ENLIL simulation (in bold) for shocks 1–6.

Table 3
2010 August ENLIL Shock Parameter Results

	v_{shock}						θ_{BN}					
	STB		Earth		*STA*		*STB*		Earth		*STA*	
	Obs.	**Sim.**	Obs.	**Sim.**	Obs.	**Sim.**	Obs.	**Sim.**	Obs.	**Sim.**	Obs.	**Sim.**
S1	470	**461**	…	…	…	…	52	**77**	…	…	…	
S2	…	…	…	…	…	…	…	…	…	…	…	
S3	626	**649**	484	**561**	…	…	72	**76**	76	**56**	…	
S4	235	**358**	…	**289**	…	…	60	**77**	…	**31.3**	…	
S5	…	…	…	…	CS	**344**	…	…	…	…	CS	**24**
S6	…	…	…	…	562	**460**	…	…	…	…	64	**46**
	v_1/v_0						n_1/n_0					
	STB		Earth		*STA*		*STB*		Earth		*STA*	
	Obs.	**Sim.**	Obs.	**Sim.**	Obs.	**Sim.**	Obs.	**Sim.**	Obs.	**Sim.**	Obs.	**Sim.**
S1	1.32	**1.22**	…	…	…	…	3.39	**2.93**	…	…	…	…
S2	…	…	…	…	…	…	…	…	…	…	…	…
S3	1.22	**1.63**	1.17	**1.19**	…	…	2.06	**1.50**	2.44	**2.79**	…	…
S4	1.08	**1.07**	…	**1.12**	…	…	3.42	**1.52**	…	**1.74**	…	…
S5	…	…	…	…	CS	**1.23**	…	…	…	…	CS	**3.78**
S6	…	…	…	…	1.53	**1.60**	…	…	…	…	5.26	**2.56**

Note. Comparison of observed and simulated shock parameters. (CS = shock occurs too close to a current sheet to accurately determine the shock parameters). Simulated parameters are shown in bold.

overtook S2 shortly after entering the ENLIL simulation; the evolution of S2 thereafter is somewhat unphysical. This result highlights a limitation of the current ENLIL modeling, which does not simulate the CME magnetic ejecta. Since there are multiple interactions between propagating CMEs, the lack of magnetic ejecta may alter the extent and the kinematic properties of the shock. To compensate for the lack of magnetic structure, the simulated cloud has pressure four times higher than that in the ambient fast wind to approximate the magnetic pressure. The lack of an internal magnetic field in the simulated cloud will reduce the "pancaking" of the rear of the cloud. The simulated cloud front models the pile-up of the plasma and magnetic field draping ahead of the CME and approximates the geometry of the CME front fairly well near CME center/nose. However, the approximation is less valid for the CME flanks/edges where the geometry would likely be different if an internal magnetic field were included.

This affects shock parameters such as the shock obliquity derived from the model. Table 3 compares the modeled shock parameters with those observed in situ. The propagation direction of S1 means that the central portion of the shock passes over *STB*. We find that values for v_{shock} and θ_{BN} (which in this case indicates a quasi-perpendicular shock) are similar to those observed. For S3 the direction of propagation results in the central portion of the CME passing closer to the Earth. The values of v_{shock} and θ_{BN} are again similar to those observed at both *STB* and *ACE*. We may have expected to see a quasi-parallel shock at *STB* since this location encounters the eastern flank of the shock. However, as mentioned earlier, Lugaz et al. (2015) find that 30% of all quasi-perpendicular shocks occur in the MC of a preceding CME. Also shown in Table 3 are values for the velocity and density jumps at the shock.

3.2. AUGSEP3 and AUGSEP4: August 14 12:00 UT to August 23 23:00 UT

AUGSEP3 was associated with CME5 that originated on the western limb of the Sun on August 14 around 09:30 UT (Bain et al. 2014). The CME propagated in a direction between Earth and *STEREO A* with LASCO plane-of-sky velocity of 989 km s^{-1}. A possible weak shock (S5) was observed at *STEREO A* at 17:50 UT on August 17 followed by a MC (M5) between 07:35 UT on August 18 and 05:11UT on August 19 (Steed & Lapenta 2011; Leske et al. 2012). The MC passage at *STEREO A* occurred during the onset of AUGSEP4.

At *STEREO B*, the proton flow throughout AUGSEP3 is predominantly away from the Sun, aligned with the magnetic field direction and persisting for several hours around the SEP onset, as shown in rows 7 to 9 of Figure 7. At *STEREO A* the 4–6 MeV proton angular distribution appears isotropic throughout, with a slight rotation in the flow direction around the peak of the SEP profile, as shown in Figure 8 rows 7–9. However, the arrival of M5 at *STEREO A* is marked by the onset of AUGSEP4 and is characterized by a departure from an isotropic angular distribution.

AUGSEP4 was associated with CME6, which originated from the same active region as CME5, on August 18, entering the LASCO field of view at 05:48 UT with a plane-of-sky velocity of 1416 km s^{-1} at 20 $R_\odot$. CME6 propagated in the direction of *STEREO A*, where a strong shock S6 was observed in situ at 16:13 UT on August 20, followed by a MC between 20:00 UT on August 20 and 20:00 UT on August 21. A reverse shock is observed at *STEREO B* at 10:27 UT on August 20, associated with an SIR rather than CME6.

The 4–6 MeV proton anisotropies during AUGSEP3/AUGSEP4 are well documented in a study by Leske et al. (2012), exhibiting a range of behaviors, including bidirectional streaming while *STEREO A* is in the MC of M5, isotropy at the tail end of the M5 time interval, and unidirectional streaming away from the Sun prior to the shock on August 20, followed by a switch to sunward-streaming particles after the passage of the shock. The bidirectional streaming, from 08:00 UT on August 18 to 01:00 UT on August 19, is evident in Figure 8 and is seen to track with the magnetic field direction as it changes in time. The event shows a particularly strong (nearly

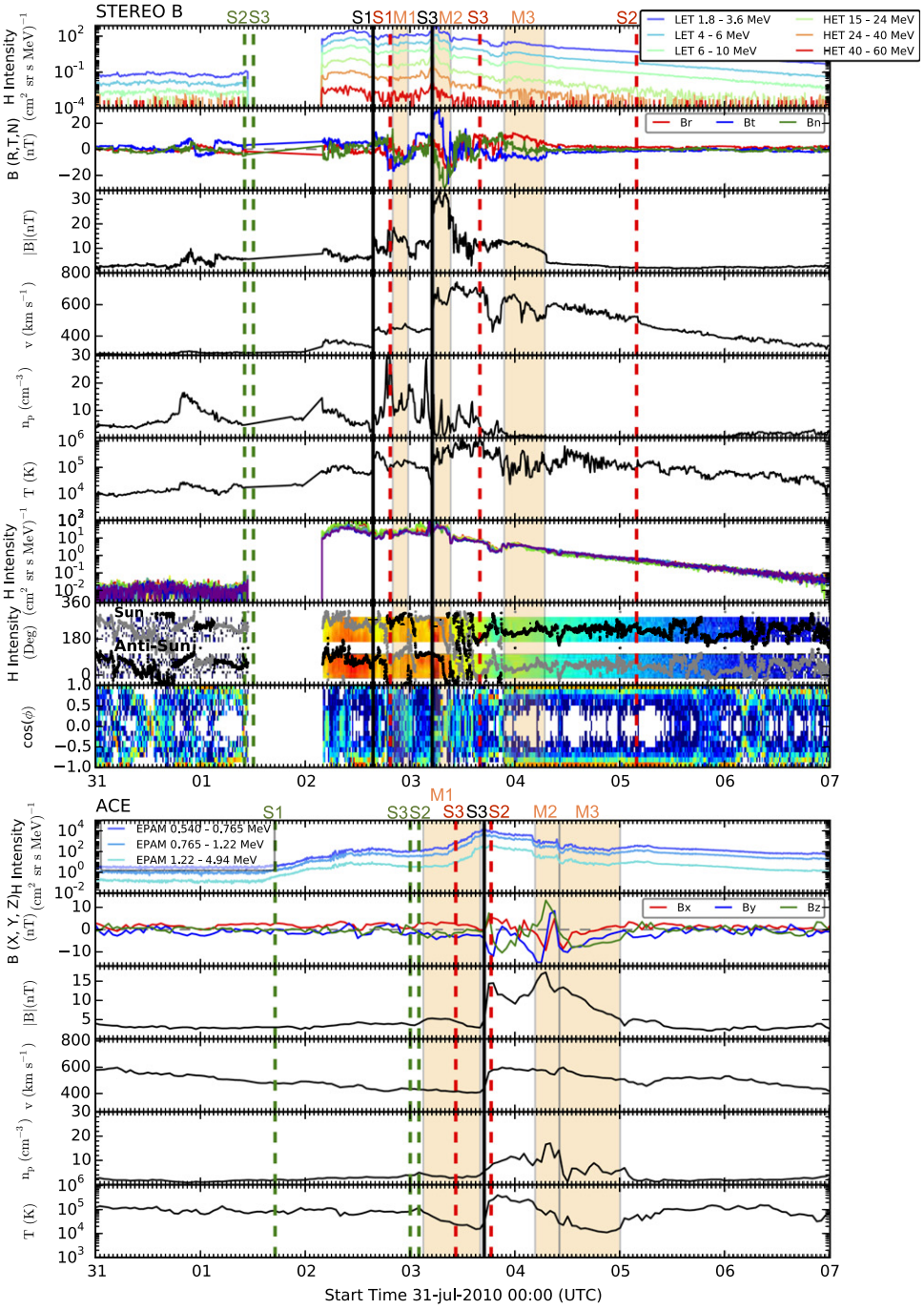

Figure 4. AUGSEP1: top and bottom panels show plasma and magnetic field data from *STEREO B* and *ACE* respectively. From top to bottom in each panel, rows show: (row 1) 1.8–60 MeV proton intensity from the LET and HET instruments on *STEREO B* (top panel) and 0.54–4.94 MeV proton intensities from EPAM on board *ACE* (bottom panel); (row 2) magnetic field components $B_{\mathrm{R,T,N}}$ from *STEREO B* and $B_{x,y,z}$ from *ACE*; (row 3) magnetic field magnitude; (rows 4–6) solar wind velocity, proton density, and temperature. From *STEREO B*: (row 7) sectored 4–6 MeV proton intensities as a function of angle with respect to the Sun from LET; (row 8) LET sector proton intensities as in row 7, plotted as in a spectrogram; gray and black lines show the radial–tangential–normal (RTN) longitude of the magnetic field ($B_{\mathrm{long}} = \tan^{-1}(B_{\mathrm{T}}/B_{\mathrm{R}})$); (row 9) LET pitch angle distribution, showing intensity as a function of $\cos(\phi)$.

$\times 1000$) enhancement in the field-aligned direction with respect to the intensity perpendicular to the field. Leske et al. (2012) suggest that the exceptional anisotropy intensities observed during M5 may be the result of enhanced particle acceleration from a possible interaction between the August 20 shock and the footpoints/legs of the preceding MC, when the shock was close to the Sun.

The bottom-right radial velocity contour plot in Figure 2 at 18:00 UT on August 18 shows the ENLIL simulation for this period. At the time of the snapshot, the western flank of CME5 can be seen grazing *STEREO A*, while CME6 can be seen inside the orbit of Mercury. In support of Leske et al. (2012), the ENLIL modeling finds that *STEREO A* is magnetically connected to a shock associated with CME6 around the time that the MC associated with CME5 would be passing the spacecraft. Furthermore, the estimated time for the first magnetic connection to S6 is well correlated with the increase in the proton intensity on August 18, at the start of AUGSEP4.

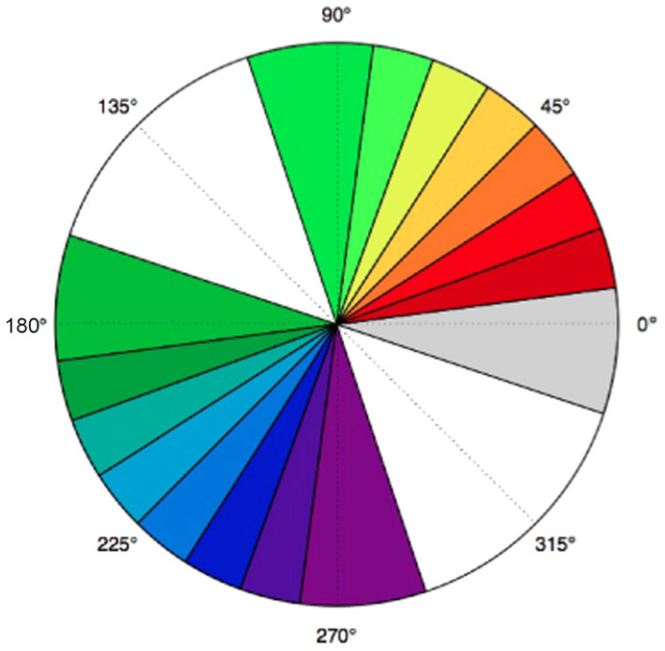

Figure 5. Viewing directions of the LET sector. Colors represent those used to plot sectored time profiles in other figures.

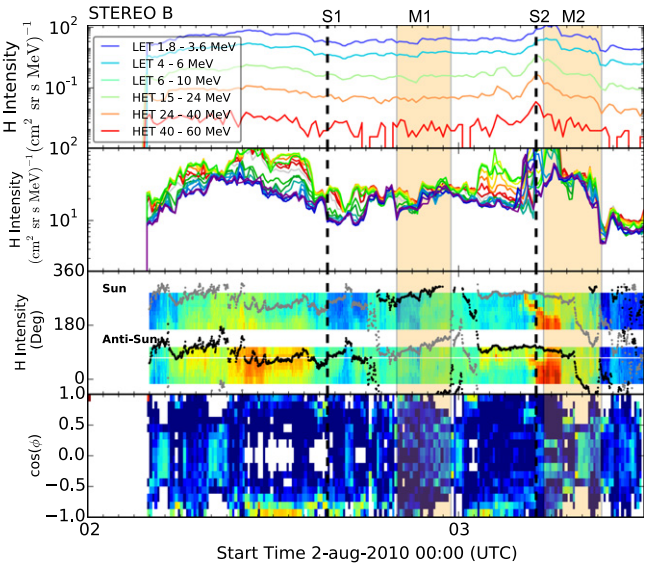

Figure 6. From top to bottom: 1.8–60 MeV proton intensity profiles from LET and HET on *STEREO B*; LET 4–6 MeV sectored proton intensities; 4–6 MeV sectored proton intensity as a function of viewing angle with respect to the Sun; and 4–6 MeV pitch angle distribution, showing relative intensity as a function of cos(ϕ).

The forecasted shock arrival derived from the model is also in good agreement with the observed arrival times for both S5 and S6 at *STEREO A*, with a disparity of less than two hours in both cases, as indicated in Table 2. However, unlike the AUGSEP1 event, the time at which *STEREO A* first became connected to S5 (and also remotely to S4 at about 2.3 AU, which continues as a weak shock following the initial connection) is not a time when the proton intensity shows an increase.

Assuming a constant propagation speed of 950 km s^{-1}, CME5 would have reached 21.5 $R_\odot$ roughly four or five hours after launch, i.e., around 14:00 UT to 15:00 UT on August 14. This time coincides with the onset of AUGSEP3 at STA, therefore it is possible that an initial connection to the shock occurred before CME5 reached 21.5 $R_\odot$. Despite this, ENLIL does not pick up a connection to S5 until much later; this may be due to the weak nature of the shock. Lowering the shock detection threshold to 10 km s^{-1} did not produce an earlier connection to S4 or S5. Alternatively we may not be simulating an accurate propagation of CME5, or the wider CME shock that is observed during the eruption, and its evolution in the background solar wind. This may represent a trade-off between optimizing the simulation to match the CME and shock arrival time and being able to correctly identify the initial connection to the shock. In this particular case, where the shock is weak, it is hard to draw firm conclusions on the performance of the model.

S5 occurs too close to a current sheet to accurately derive shock parameters from the observations (labels CS in Table 2). The modeled shock parameters for S6 are in reasonable agreement with the observed values. The simulated shock velocity is within ~20% of the observed value and θ_{BN} is found to be oblique for both observations and the model. The jump in shock velocity is found to be comparable, but the jump in density is not, indicating that the shock or background solar wind density has not been accurately modeled for this case. The ENLIL-modeled CME has an artificially higher pressure to make up for not having a strong magnetic field. This could be leading to the higher density ratios in the model.

Despite corresponding intensity increases for AUGSEP3 and AUGSEP4 at *ACE* and *STEREO B*, the model did not identify any remote connections to S5 at *STEREO B*, or for S6 at *ACE* or *STEREO B*. The direction of CME6 points to 42° west of the Earth. At that time *STEREO B* was 72°.4 east of the Earth, and thus CME6 was 114° west of *STEREO B*, about 24° behind the west limb from the spacecraft perspective. It is therefore unlikely that *STEREO B* would observe an SEP in this configuration for a fast CME such as CME6. It seems that the fitted CME parameters are not wide enough to form a remote shock connection to S6 from *STEREO B* in the ENLIL simulation. However, an EUV wave was seen to wrap around the limb such that it was observed on disk from the *STEREO B* EUVI instrument. It is beyond the scope of this paper to investigate the exact relation of the shock to the EUV wave, except to say that this suggests the shock may be wider than measured with the GCS fitting. Alternatively *ACE* and *STEREO B* might only be connected to S5 or S6 while they are inside the ENLIL inner boundary.

3.3. Summary of 2010 August Modeling

In general, ENLIL modeling did a good job of estimating when the observer first became magnetically connected to the shock. Eight of the 14 estimates of first connectivity occurred close to an increase in the proton intensity, to within a few hours. For three shock connections, i.e., S1, S2, and S3 at *STA*, the observer first becomes connected to the shock once it has gone beyond 2 AU, and it is unclear if any of these shocks are strong enough for us to expect an increase in the proton intensity observed, but there is a gradual increase in the proton intensity at *STEREO A* around this time.

For all six local shocks observed by the spacecraft, the model correctly identified a local shock arriving within 7–14 hr of the observed CME shock arrival time, as expected from WSA-ENLIL + Cone modeling (Millward et al. 2013; Mays et al.

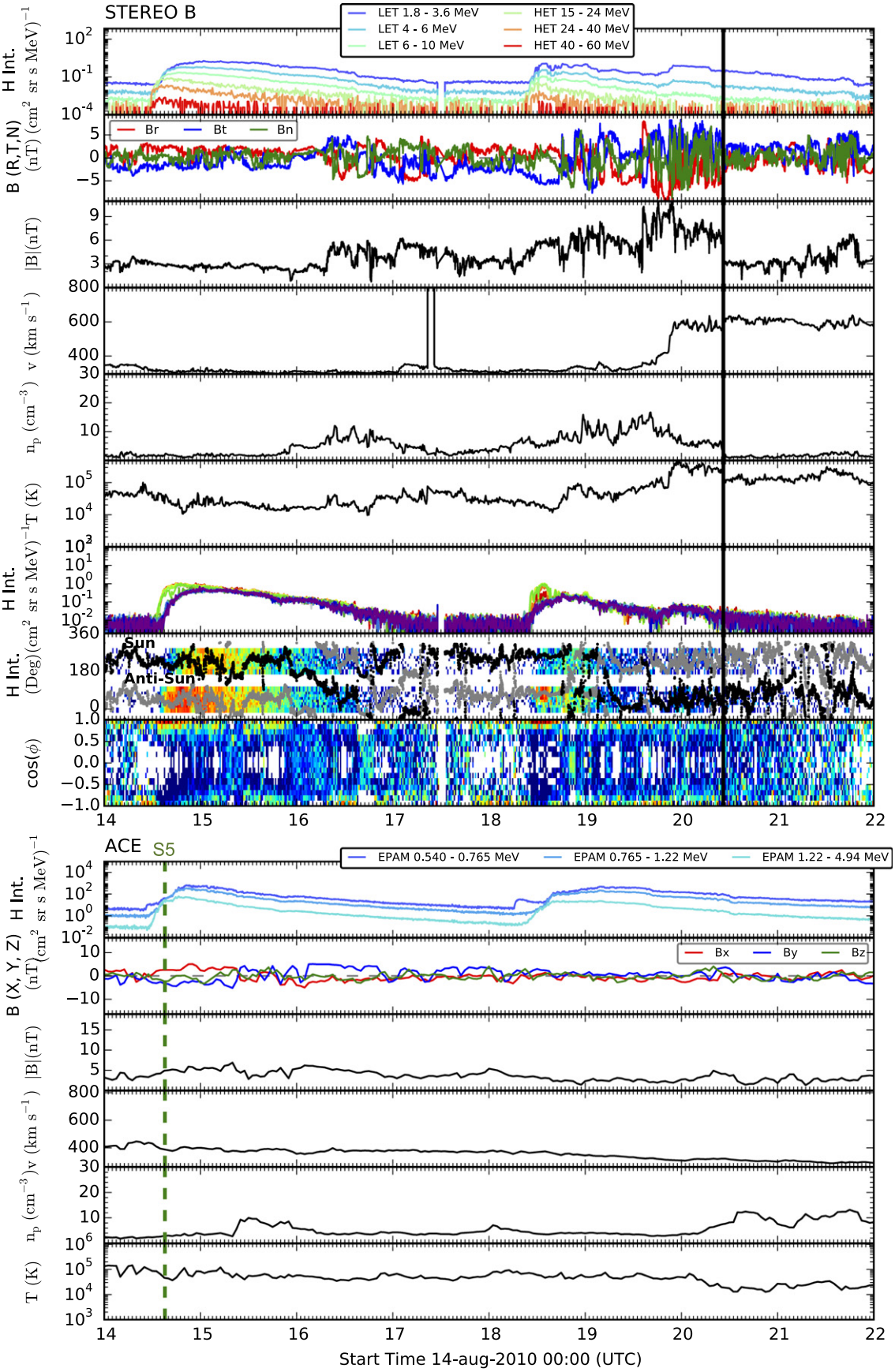

Figure 7. Plasma and magnetic field observations of AUGSEP3 and AUGSEP4 at *STEREO B* (top panel) and *ACE* (bottom panel). The figure format follows that of Figure 4.

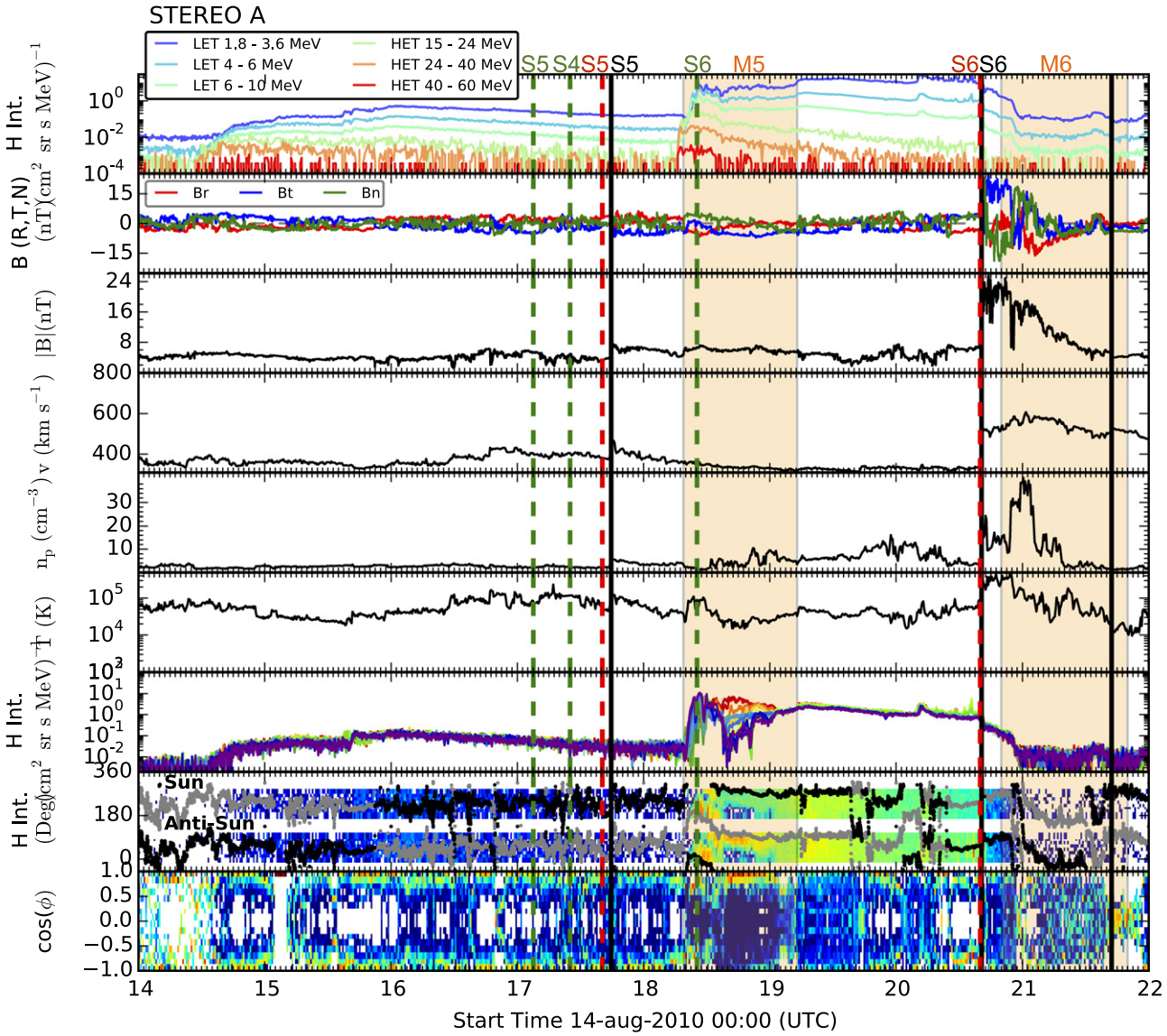

Figure 8. Plasma and magnetic field observations of AUGSEP3 and AUGSEP4 at *STEREO A*. The figure format follows that of the top panel of Figure 4 for *STEREO B*.

2015). While still within this acceptable 7–14 hr timeframe, the largest disparity between the modeled and observed shock arrival times was found for AUGSEP1. Many tweaks to the ENLIL model parameters were tested including increasing the cloud density ratio, which helped to some degree. The modeled solar wind speed at *STEREO B* is greater than observed, which could have some effect; however, it is likely that the inability of the model to simulate the magnetic ejecta and consequently the magnetic interaction between CMEs contributes to the discrepancy. In particular, the lack of magnetic ejecta in the model will play into the preconditioning of the background environment in which subsequent CMEs propagate. For the modeled time period there was one "false alarm," i.e., S4 at *ACE*, where the model predicted a shock arrival at *ACE* that was not verified by the observations. However, given the direction and width of CME propagation, it is possible that *ACE* just missed observing the shock since it would have encountered the very edge/flank of the CME. Alternatively, due to the absence of the magnetic ejecta, the CME flank can be unrealistically modeled.

4. 2012 JULY EVENTS

Our second case study covers the period from 2012 July 12 to 31. Figure 9 shows a summary of the proton intensity profiles at *STEREO A*, *STEREO B*, and *ACE* for this period, with the vertical lines representing the observed (black solid) and modeled (green: observer's first magnetic connection to the shock; red: shock passage) shock connections, as before. An overview of the SEP events (labeled JULSEP1–JULSEP4) and their associated CME(s) (labeled CME1–CME5) is detailed in Table 4, which follows the same format as Table 1. Also listed are the observed shock arrival times at each spacecraft, corresponding to those marked in Figure 9, which are labeled S1–5 in accordance with the corresponding CME numbering.

Figure 10 shows a series of snapshots of radial velocity contours (cropped to 2 AU from a 5.5 AU run for clarity) taken throughout the 20 day ENLIL model run beginning on 2012 July 12. For this period a time-dependent inner boundary was created from a series of daily input WSA synoptic maps each computed from a new GONG daily synoptic magnetogram

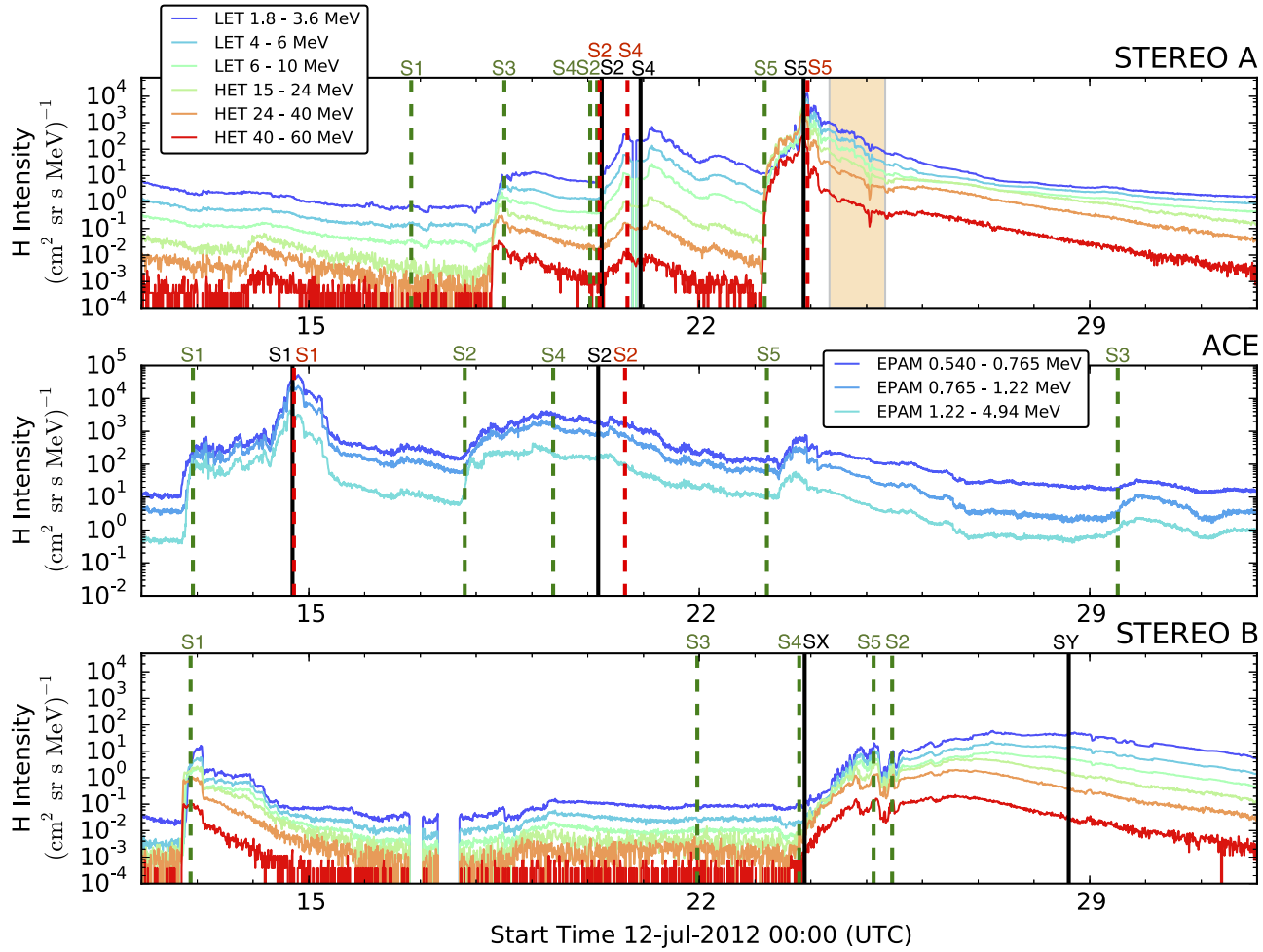

Figure 9. Proton time profiles from the *STEREO* LET and HET (*STEREO A*: top and *STEREO B*: bottom) and ACE EPAM (middle) instruments for the 2012 July period of SEP events. Black vertical solid lines indicate shock arrivals at the spacecraft, numbered to reference the CME numbers defined in Table 4. Orange shaded time periods indicate magnetic cloud passages observed at the spacecraft. Green vertical dashed lines indicate the times when the spacecraft first becomes magnetically connected to the shock as simulated by ENLIL modeling. Red vertical lines indicate the ENLIL-predicted shock arrival time at each spacecraft. ENLL shock connections are also numbered with reference to the CME numbers defined in Table 4.

every 24 hr at the ENLIL inner boundary. The default ENLIL CME density ratio factor (dcld) of 4 was used for CMEs 1–4, with a factor of 8 used for CME5. An elongation factor (xcld: the ratio of the radial CME width to the spherical CME width) of 1 was used for CMEs 1–4 and a factor of 4 was used for CME5, where xcld = 1 is a sphere and xcld = 2 is a sphere where the trailing end is elongated by a factor of two in the radial direction. Figure 11 shows the corresponding shock connections, solar wind, and shock parameters ($v_{\rm shock}$, n_1/n_0, v_1/v_0, $\theta_{\rm BN}$) for the July simulation. Details of the remote shock connection times and shock arrival at each spacecraft, as simulated by ENLIL, are listed in Table 5.

4.1. JULSEP2, JULSEP3, and JULSEP4: 2012 July 17 12:00 UT to July 31 23:59 UT

The period from July 17 to 20 consisted of three fast CME eruptions with velocities greater than 800 km s^{-1}, defined here as CME2, CME3, and CME4, and listed in Table 4. CME2 was first observed in the LASCO C2 field of view at 13:48 UT on July 17 with a plane-of-sky velocity of 1319 km s^{-1} at 20 $R_\odot$. This is followed on July 18 by CME3, which first entered the field of view of LASCO C2 at 06:24 UT with a velocity of 806 km s^{-1} at 20 $R_\odot$, and then by CME4 on July 19 at 05:24 UT. With a greater velocity of around 1600 km s^{-1}, CME4 catches up and interacts with CME2 on its western flank and CME3 on its eastern flank, as shown in Figure 10.

Propagating in the direction of *STEREO A*, the shock associated with CME3 appears to be responsible for generating JULSEP2. ENLIL modeling finds *STEREO A* to have a remote connection to S3 at 12:08 UT on July 18, occurring when the shock is close to the ENLIL inner boundary at 21.5 $R_\odot$, Figure 12. The timing of this first connection to the shock occurs several hours after the observed SEP onset, suggesting that the model missed the initial connection to the shock, which appears to have occurred closer to the Sun than the ENLIL inner boundary. Later, on July 20 at 16:01 UT, a shock is observed at *STEREO A*. According to the ENLIL modeling, this shock is associated with the very end of the flank of CME2. However, around this time, in the simulation, the flanks of CME2 and CME3 are merging in the region of *STEREO A*; see Figure 10 (radial velocity plot, top right). It is therefore not clear which of these two CMEs (or perhaps a merged structure of the two) the observed shock is truly associated with. At *STEREO A*, JULSEP3 begins during the decay of JULSEP2. The SEP event has a double peak that is punctuated with a shock arrival at 22:43 UT on July 20, which ENLIL attributes

Table 4
2012 July SEP Events

SEP	Start Time (UT)	End Time (UT)	CME					Shock Arrival		
			No.	Start Time (UT)	Velocity (km s^{-1})	Lat. (deg)	Long. (deg)	*STB* (UT)	Earth (UT)	*STA* (UT)
JULSEP1	Jul 12 20:00	Jul 16 00:00	CME1	Jul 12 16:48 (19:29)	2265* (1300)	−15	7	⋯	Jul 14 17:27	⋯
JULSEP2	Jul 17 21:00	Jul 20 09:00	CME3	Jul 18 06:24 (10:32)	806* (840)	4	166	⋯	Jul 20 04:18x	⋯
JULSEP3	Jul 20 09:00	Jul 23 06:00	CME2	Jul 17 13:48 (18:40)	1319* (850)	−30	62	⋯	⋯	Jul 20 06:01
			CME4	Jul 19 05:24 (07:40)	1616* (1600)	−14	90	⋯	⋯	Jul 20 22:34
JULSEP4	Jul 23 06:00	Aug 1 00:00	CME5	Jul 23 02:36 (03:50)	1972* (2500)	2	125	Jul 23 21:21Jul 28 14:58	⋯	Jul 23 20:55

Note. Column 1 labels each SEP event in the July series, with start and end times defined in Columns 2 and 3. Columns 4–8 contain information on the CME(s) associated with each SEP event. Column 4: CME label. Column 5: CME observed start time (events marked † indicate CME start times taken from the literature and explicitly mentioned in the text below, * indicate start times taken from the LASCO CME catalog http://cdaw.gsfc.nasa.gov/CME_list/, when the CME leading edge first appears in the C2 field of view), and in brackets the time that the CME enters the ENLIL simulation at 21.5 $R_{\odot}$. Column 6: CME initial velocity (events marked † indicate CME initial velocities taken from the literature, * indicate the second-order speed at 20 $R_{\odot}$, from plane-of-sky measurements of the CME, taken from the LASCO CME catalog), in brackets is the CME velocity used as an input to the ENLIL modeling, determined using 3D reconstructions of the CME front from multipoint WL coronagraph observations. Columns 7 and 8: latitude and longitude of CME origin. Columns 9–11 list shock arrival times at *STEREO B*, Earth, and *STEREO A*.

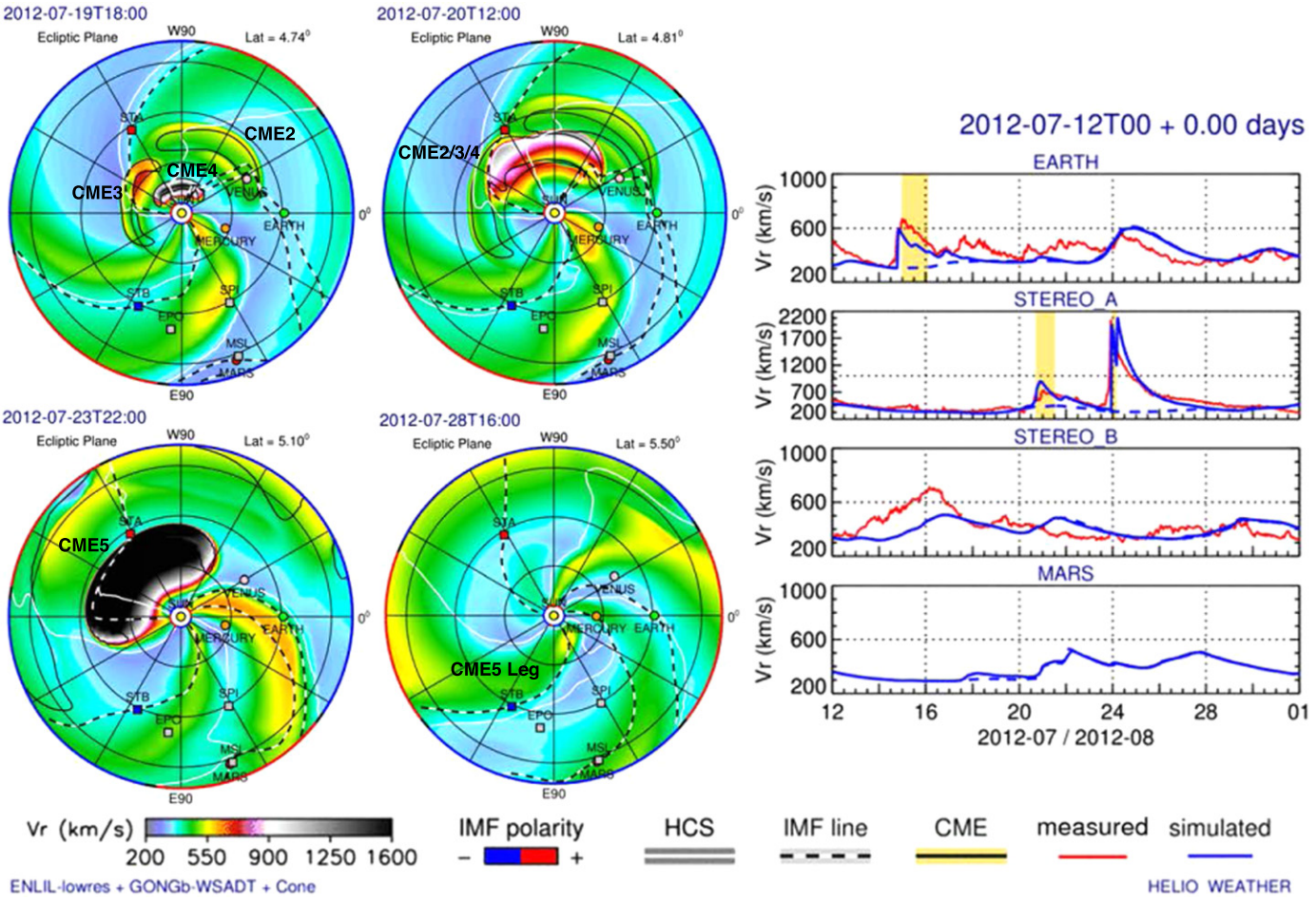

Figure 10. Left: radial velocity contour plots at four times during the ENLIL 2012 July simulation run, cropped to 2 AU. Black and white dashed lines show the simulated magnetic connectivity of each spacecraft to structures in the heliosphere. Right: profiles of the observed (red) and simulated (blue) radial solar wind velocity at Earth, *STEREO A*, *STEREO B*, and Mars.

to the shock from CME4. At Earth we did not observe two distinct SEP events, i.e., JULSEP2 and JULSEP3; instead we see a gradual event beginning around 17:00 UT on July 17 (Figure 9). This gradual event is associated with the shock from CME2, with a possible additional superposed component resulting from a remote connection with CME4.

In general, despite the complexity of the interacting CMEs, the model does a good job in simulating the macroscopic behavior of this time period at *STEREO A*, capturing the timing of all three of the observed shocks within <6 hr of the shock passage, and also in matching the observed radial velocity of the solar wind; see Figure 10 (right panel) and Tables 5 and 6. However, at Earth the model performed less well in its estimate of the solar wind velocity at *ACE* for JULSEP2, and the predicted shock arrival for S2 occurs 12 hr after the observed shock. This may be because *ACE* encounted only the flank of CME2 and there could be some ambiguity in the measured width of the CME. The simulation also does a good job of modeling the shock properties, accurately matching the shock velocity and providing comparable values for θ_{BN} in most cases, Table 6.

While the interaction of CMEs 2–4 is complex, it is clear that the preconditioning of the interplanetary medium through the interaction of these CMEs was an important precursor to the subsequent SEP event (JULSEP4). The July 23 CME that followed (CME5 in our study) has resulted in several papers (Cash et al. 2013; Russell et al. 2013; Liu et al. 2014; Temmer & Nitta 2015). This extremely fast event was one of the most energetic CMEs ever recored, with a maximum speed of 3050 km s^{-1}; it arrived at *STEREO A* in just 18.6 hr (and at 1 AU in 21 hr) (Liu et al. 2014). In situ monitors at *STEREO A* recorded a shock arrival speed greater than 2200 km s^{-1} and an unusually intense magnetic ejecta with a field strength of 109 ± 1 nT. Liu et al. (2014) attributed the fast transit time to an uncharacteristically slow deceleration. The authors suggested that the CME was propagating into a region of low solar wind density in the interplanetary medium, combined with an increase in the solar wind speed, as a result of preconditioning by an earlier CME(s) in the previous few days, i.e., CMEs 2, 3, and 4 in this study. Liu et al. (2014) goes further, to suggest that the strong ejecta was the result of a CME–CME interaction close to the Sun, as two filament eruptions occurred in close succession over 10–15 minutes. The CME propagation was toward *STEREO A*, but had the CME been directed at Earth the outcome would have been a severe geomagnetic storm (Baker et al. 2013; Ngwira et al. 2013).

The ENLIL modeling of JULSEP4 is in good agreement with observations for *STEREO A*. The simulation finds *STEREO A* to have a remote connection to S5 at 04:09 UT on July 23, as the CME enters the ENLIL inner boundary. The timing of this is in good agreement with the onset of JULSEP4, suggesting that the spacecraft first becomes connected to S5 at

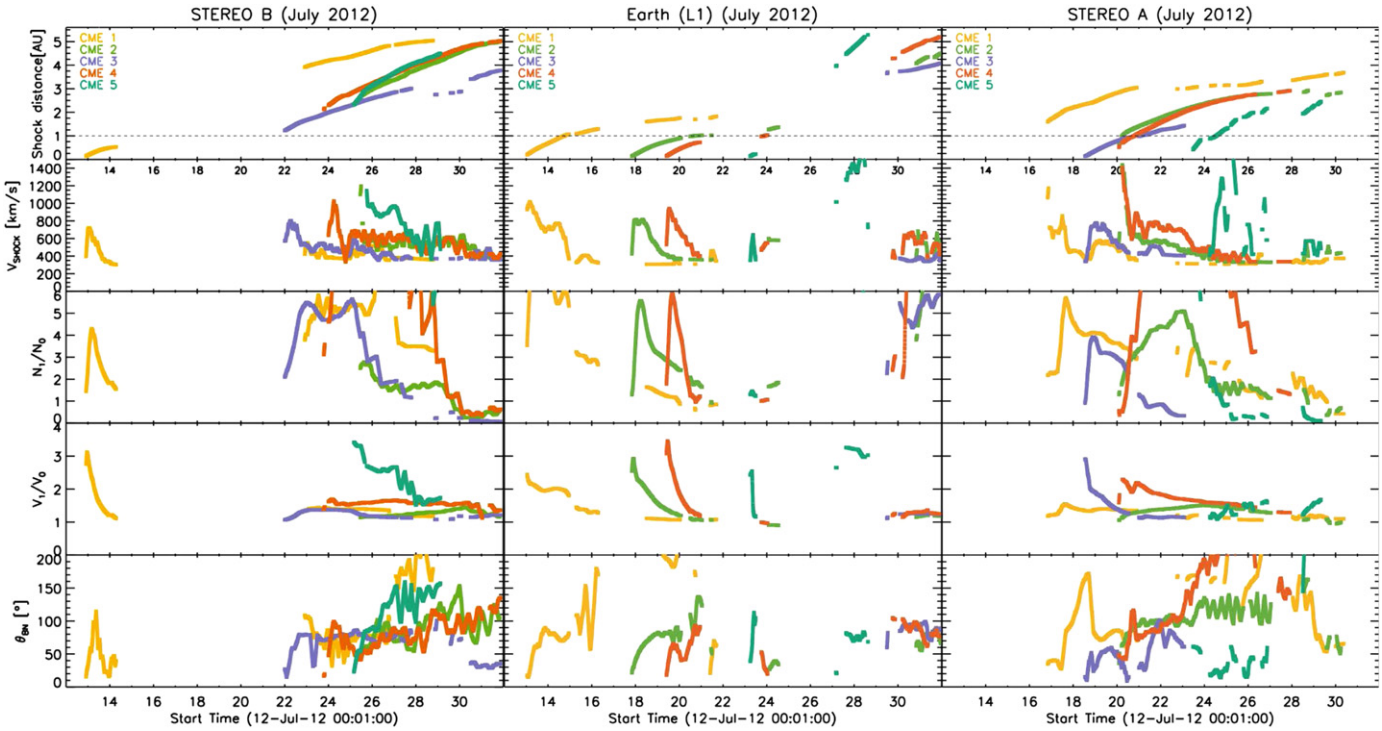

Figure 11. From ENLIL modeling of the 2012 July periods, the top row of each plot shows periods when *STEREO B* (left), Earth/*ACE* (middle), and *STEREO A* (right) were connected to shocks associated with CMEs 1–6 and the shock distance from the Sun at that time. Rows 2–5 show the shock and solar wind properties at the shock on the spacecraft-connected field line: the shock velocity (row 2); the ratio of the solar wind density n_1/n_0 up- and downstream of the shock (row 3); the ratio of the solar wind velocity v_1/v_0 up- and downstream of the shock (row 4); and θ_{BN}, the angle between the shock normal and the interplanetary magnetic field.

slightly less than 21 $R_\odot$. Furthermore, the simulated shock arrival at *STEREO A* is in agreement with the observed shock passage to within an hour and 40 minutes, and the ENLIL-determined shock speeds of $\sim$1900 km s^{-1} are in close agreement with the observed shock velocity of $\sim$2200 km s^{-1}. Due to the intensity of the event, PLASTIC suffered a data gap at the peak of the SEP. A value for the velocity jump is taken from Temmer & Nitta (2015), where plasma parameters were reconstructed from the 5 minute magnetic field data.

Despite remote magnetic connections to each of the CMEs, ENLIL finds no counterpart to the two shocks observed in situ on July 23 (SX) and July 28 (SY), at *STEREO B*, Figure 13. From the plot of the radial velocity of the solar wind at 22:00 UT on July 23, i.e., Figure 10 (bottom left), it is hard to envision how the shock associated with CME5 can produce the SX shock at *STEREO B*. The shock would need to be significantly wider than the white-light CME leading edge that is used as an input to the model. The left flank of the hydrodynamic disturbance of CME5 is around 30° east of *STEREO B* when SX is observed at the spacecraft. It is most likely that SX is driven by an ICME associated with a small faint CME that left the Sun on July 19 around 05:30 UT with a plane-of-sky speed of around 275–350 km s^{-1}. From a 3D triangulation the CME was found to be at $-125°$ longitude and $-20°$ latitude. Traveling in this direction at a constant speed of 350 km s^{-1}, the CME would arrive at *STEREO B* within seven hours of SX. Based on our selection criteria, this CME was not fast enough to be included in the ENLIL simulation, and while there is a nice EUV signature for the CME, it is not so clear in the white-light coronagraph images. It is possible that the remote connection from *STEREO B* to the merged structure of CMEs 2–4, identified in the simulation out at 2–3 AU, also contributes to the JULSEP4 profile at *STEREO B*.

Leske et al. (2014) identified a loss-cone distribution present at *STEREO B*, observed by LET for 1.8–10 MeV protons, on July 24 and 25; see panels 8 and 9 of Figure 13. Loss-cones such as this are caused by mirroring of particles in a magnetic bottle. Only particles with small pitch angles make it through the bottleneck, while those with large pitch angles are reflected. The authors attribute the distribution to energetic protons flowing back toward the Sun from behind the shock. While ENLIL does not observe S5 in situ, the model does support this loss-cone hypothesis, with a remote connection to S5 once the shock reaches 2.27 AU.

While the shock, SY, observed on July 28 at 14:59 UT at *STEREO B* is not generated by the simulation, it is seen from the plot of the radial velocity of the solar wind for this time (Figure 10, bottom right) that a structure associated with the leg of CME5 passes *STEREO B* at this time, and hence we refer to this as S5′. A current limitation of the model in picking out multiple shocks associated with the same structure may have resulted in this shock being missed. Ongoing developments to the model will address this in future.

4.2. Summary of 2012 July Modeling

Of the 15 remote shock connections identified in the simulation for 2012 July, 10 occurred at or within a few hours of an increase in the proton intensity profile. A few other cases were ambiguous, sometimes occurring during the rise or decay of a previous event when the shock may not have been strong enough to produce a noticeable increase superimposed on the already occurring SEP. Once again we see that a number of these remote connections occur beyond 1 AU, roughly a third

Table 5
2012 July ENLIL Shock Connectivity Results

Shock	First Shock Connection			Shock Arrival					
	STB UT (AU)	Earth UT (AU)	*STA* UT (AU)	*STB* (UT)		Earth (UT)		*STA* (UT)	
				Obs.	**Sim.**	Obs.	**Sim.**	Obs.	**Sim.**
S1	Jul 21 21:08 (0.12)	Jul 12 22:07 (0.13)	Jul 16 20:04 (1.59)	…	…	Jul 14 17:27	**Jul 14 17:37**	…	…
S2	Jul 25 11:06 (2.65)	Jul 17 19:06 (0.12)	Jul 20 04:03 (0.92)	…	…	Jul 20 04:18	**Jul 20 16:03**	Jul 20 06:01	**Jul 20 05:07**
S3	Jul 21 23:10 (1.21)	Jul 29 12:02 (3.65)	Jul 18 12:08 (0.13)	…	…	…	…	…	…
S4	Jul 23 19:00 (2.13)	Jul 19 09:08 (0.12)	Jul 20 01:03 (0.46)	…	…	…	…	Jul 20 22:43	**Jul 20 17:06**
SX/S5	Jul 25 03:01 (2.27)	Jul 23 05:06 (0.12)	Jul 23 04:09 (0.13)	Jul 23 21:21	…	…	…	Jul 23 20:55	**Jul 23 22:35**
SY/S5′	…	…	…	Jul 28 14:59	…	…	…	…	…

Note. Left columns list the time when each spacecraft first becomes magnetically connected to each shock from CMEs 1–5, with the radial distance in brackets. Right columns show the observed shock arrival times and the predicted arrival time from the ENLIL simulation (in bold) for shocks 1–5.

Table 6
2012 July ENLIL Shock Parameter Results

	v_{shock}						θ_{BN}					
	STB		Earth		*STA*		*STB*		Earth		*STA*	
	Obs.	**Sim.**	Obs.	**Sim.**	Obs.	**Sim.**	Obs.	**Sim.**	Obs.	**Sim.**	Obs.	**Sim.**
S1	⋯	⋯	470	**594**	⋯	⋯	⋯	⋯	76	**72**	⋯	⋯
S2	⋯	⋯	370	**364**	383	**411**	⋯	⋯	40	**79**	44	**63**
S3	⋯	⋯	⋯	⋯	⋯	⋯	⋯	⋯	⋯	⋯	⋯	⋯
S4	⋯	⋯	⋯	⋯	652	**617**	⋯	⋯	⋯	⋯	24	**60**
S5	382	…	⋯	⋯	2200+[†]	**1940**	40	…	⋯	⋯	46	**24**
	410	…	⋯	⋯	⋯	⋯	44	…	⋯	⋯	⋯	⋯
	v_1/v_0						n_1/n_0					
	STB		Earth		*STA*		*STB*		Earth		*STA*	
	Obs.	**Sim.**	Obs.	**Sim.**	Obs.	**Sim.**	Obs.	**Sim.**	Obs.	**Sim.**	Obs.	**Sim.**
S1	⋯	⋯	1.40	**1.97**	⋯	⋯	⋯	⋯	2.48	**5.98**	⋯	⋯
S2	⋯	⋯	1.20	**1.06**	1.23	**1.12**	⋯	⋯	3.15	**1.75**	4.05	**1.77**
S3	⋯	⋯	⋯	⋯	⋯	⋯	⋯	⋯	⋯	⋯	⋯	⋯
S4	⋯	⋯	⋯	⋯	1.18	**1.93**	⋯	⋯	⋯	⋯	1.82	**3.90**
S5	1.13	…	⋯	⋯	∼2.2[†]	**1.21**	2.28	⋯	⋯	⋯	DG	**1.80**
	1.13	…	⋯	⋯	⋯	⋯	3.32	…	⋯	⋯	⋯	⋯

Note. Comparison of observed and simulated shock parameters. (DG = data gap, [†] Temmer & Nitta 2015). Simulated parameters are shown in bold.

of all cases in the July period, indicating that it is important to consider the influence of shocks beyond the spacecraft. However, we point out that often the shock has considerably weakened beyond 1 AU, and it is connections to the CME shocks within 1 AU that cause the major SEP events.

Of the seven shocks observed at the spacecraft during this period, the model correctly captured five shock arrivals, all within the 7–14 hr expected from ENLIL modeling. All but one of these captured shocks occurred within 6 hr of the observed shock. Of the remaining two shocks observed at *STEREO B* on July 23 and 28, the first was associated with a CME that was traveling too slowly to pass our selection criteria and be included in the simulation, and the second was likely missed due to a limitation of the model, which currently does not identify multiple shocks associated with the same structure.

From studying this period, we find from the ENLIL results the importance of considering the preconditioning of the heliosphere in the days before an SEP event. The July 23 SEP is a prime example of this, and our results support the findings of other authors.

5. DISCUSSION

For the two case studies in this paper, ENLIL modeling was carried out in a "forward modeling" manner, where ENLIL parameters were tweaked in order to best match the observations, and the simulated results considered a success if a match between the observed and modeled shock arrival times was achieved. In certain situations limitations with the current model may have prevented a better match.

1. Currently the ENLIL inner boundary is 21.5 $R_\odot$. In several cases the observer is already connected to the shock as it enters the simulation range and we are missing the initial connection to the shock when this occurs below 21.5 $R_\odot$. Future development of the model would seek to pair the simulation with a coronal propagation model.
2. The CMEs propagating in the ENLIL model do not contain an internal magnetic structure, which may affect the CME kinematics and its interaction with other structures. This may account for the small discrepancies seen in the 2010 August events, where merging CMEs still maintain identifiably distinct magnetic structures.
3. The CME input parameters are obtained from fits to the CME leading edge observed in EUV and white-light images. While this describes the shock driver, the shock itself may be much wider than the fitted CME.

In some cases the observer's local connection to the shock matched the observations but the observer's first identifiable remote connection to the shock did not occur at or close to (allowing for a time delay, due to the initial connection happening within 21.5 $R_\odot$) the onset of the SEP event, e.g., AUGSEP3 at *STEREO A* for S4 and S5. This may represent a situation where the kinematics of the propagating CME were not well modeled, or, alternatively, this may suggest that the observer does not need to be magnetically connected to the shock in order to produce a SEP. In such a case, cross-field transport of the particle flow via diffusion mechanisms may play a role. MacNeice et al. (2011) carried out a validation of the WSA-ENLIL model and its ability to correctly determine field line connections to active regions that produced flares related to prompt SEPs, finding that the performance is similar to the assumption of a simple Parker spiral model. The authors consider the main source of inaccuracy to result from the use of static synoptic magnetograms, unreliably modeling the transient low coronal activity and in turn inaccurately reproducing the low-latitude open flux. Their suggestion of using a time-dependent input at the ENLIL boundary was implemented for our case study of the 2012 July SEP events.

Despite these considerations, we were able to find a good fit to the majority of events in the two case studies. Particularly in the presence of multiple ejecta occurring in quick succession, representative of the activity level at solar maximum, the preconditioning of the heliosphere and the interplay of these structures can strongly influence the SEP profiles. Heliospheric models such as WSA-ENLIL provide essential contextual information, particularly as connectivity to shocks beyond

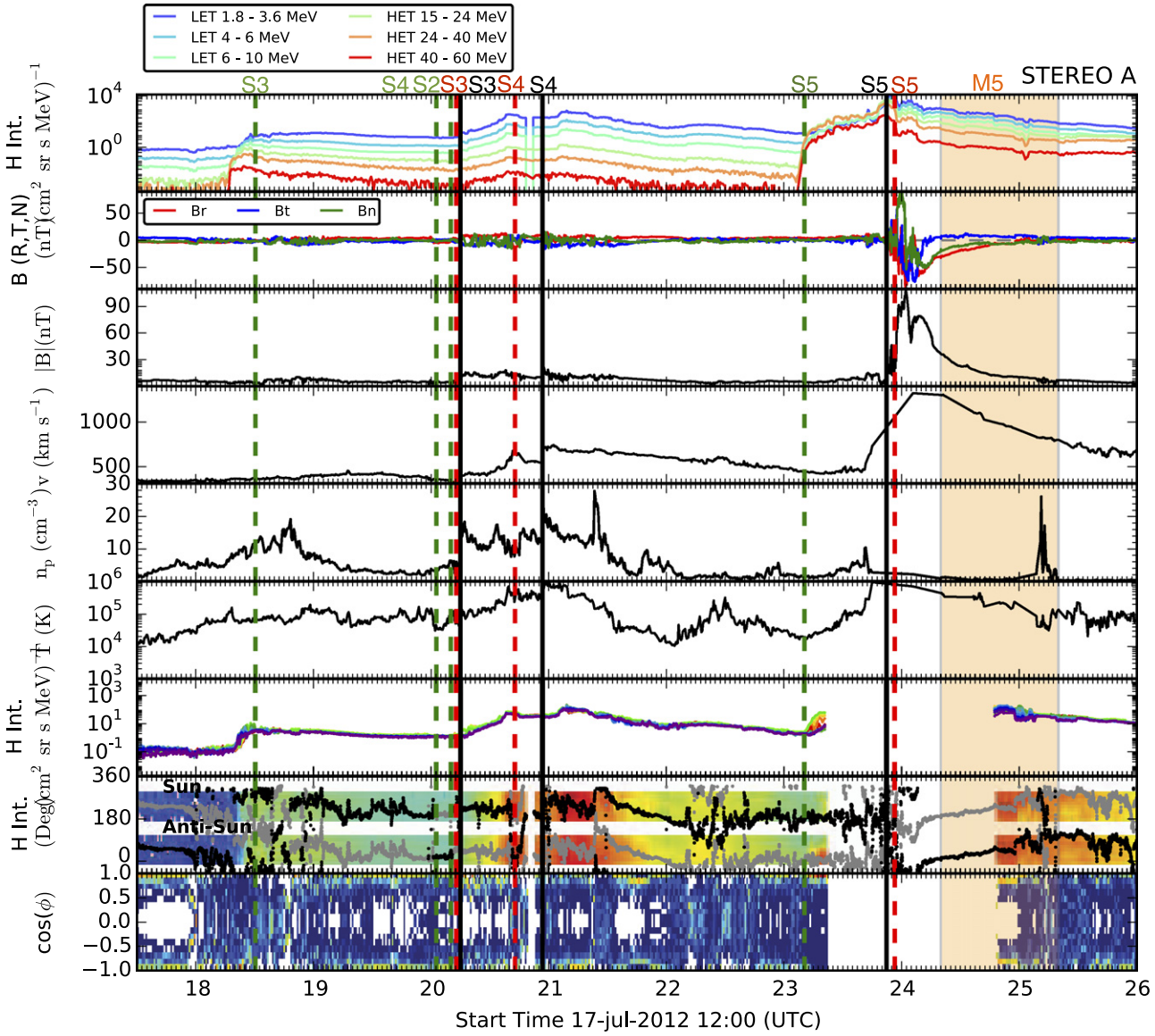

Figure 12. Plasma and magnetic field observations of JULSEP2, JULSEP3, and JULSEP4 at *STEREO A*. The figure format follows that of the top panel of Figure 4 for *STEREO B*.

1 AU is a common occurrence and can be attributed to some of the weak increases in particle intensities observed at the spacecraft.

6. CONCLUSIONS

Focusing on the SEP-rich periods of 2010 August and 2012 July, we identified fast CMEs that were likely to have produced shocks that directly or indirectly (through preconditioning of the interplanetary medium) influenced the SEP profiles observed in situ at *STEREO A*, *B*, and Earth/*ACE*. CME-fitted parameters were used as an input to WSA-ENLIL + Cone models spanning the duration of each period. From the model, remote and local magnetic shock connections to each spacecraft were identified and compared with SEP timing and intensity profiles, and the accompanying in situ plasma and magnetic signatures. Interpreting these profiles in the context of a realistic heliospheric background through which the CMEs were propagating proved to be essential for understanding the complex SEP profiles in these two case studies, particularly when there are multiple ejecta, representative of solar maximum. Knowledge of the observer's connection to the shock, and other solar wind structures, will prove to be a vital component when investigating the longitudinal extent of SEP events and the interplay with cross-field transport of the particles.

The possibilities for using ENLIL shocks in the above manner for forecasting SEP events, based on the results shown, are clear. However, our final fitting of the observations, including both local shocks and remote connections, often required several adjustments to the originally derived cone parameters from the coronagraph images. Thus forecasts are likely to have less fidelity. Nevertheless, the ability to have some knowledge ahead of time of a strong shock connection is available if the heliospheric model with CMEs is run immediately upon tracking a fast CME, and later on the likelihood of arrival of a strong SEP enhancement can be inferred. This represents a new capability for space weather

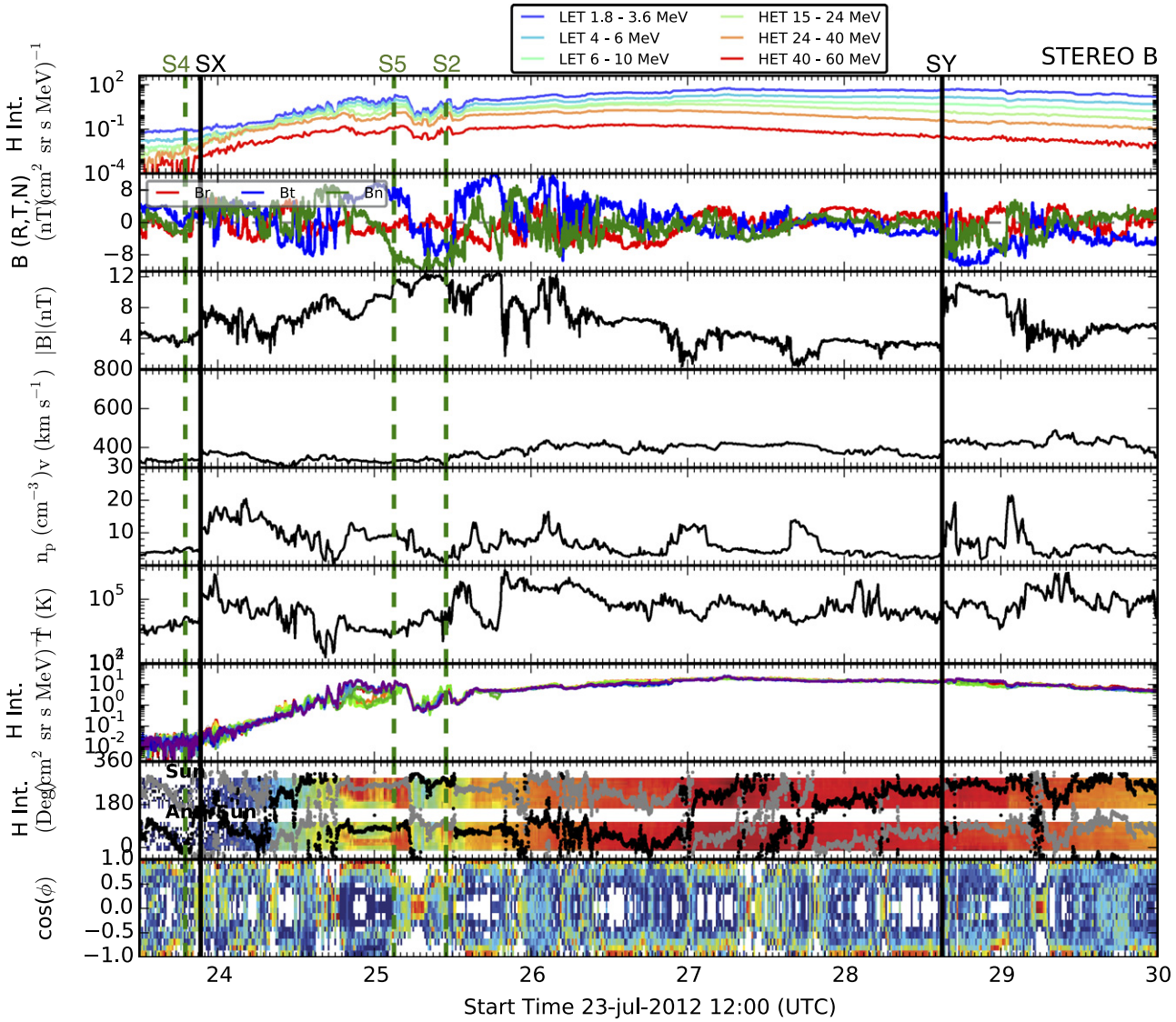

Figure 13. Plasma and magnetic field observations of JULSEP2, JULSEP3, and JULSEP4 at *STEREO B*. The figure format follows that of the top panel of Figure 4.

resources in an area that has long needed updated tools. The NASA Space Weather Research Center (http://swrc.gsfc.nasa.gov/main/) is preparing to serve such shock results in the near future as a routine ENLIL product.

From a physics standpoint, these results demonstrate that even the simplified treatment of the heliospheric shock drivers in ENLIL can provide useful knowledge related to the SEP environment. Moreover, the success of our interpretations of the complex SEP event periods in 2010 August and 2012 July in terms of connections to shock sources and parallel propagation alone suggest that these assumptions have a basic validity that holds regardless of the complexity of the conditions. In many ways these results further support the early work with this concept by Kallenrode & Wibberenz (1997) and Lario et al. (1998), but go a step further in their use of a state-of-the-art, data-driven heliospheric model. Further progress can be made by adding the coronal portions of the shocks and observer connections, and by introducing more realistic CME ejecta into the picture. These coupled needs may soon be realized in view of work underway to simulate the detailed CME process (e.g., Torok et al., Manchester et al., Lugaz et al.)

This work was supported by the IMPACT Investigation grant (NAS503131), by NASA ROSES LWS grant NNH14ZDA001NLWS and NNX15AB80G, and by NSF grants AGS 1259549 and 1321493. Simulation results have been provided by the Community Coordinated Modeling Center at Goddard Space Flight Center through their public Runs on Request system (http://ccmc.gsfc.nasa.gov; run numbers Leila_Mays_052715_SH_1, Leila_Mays_033115_SH_1). The WSA model was developed by N. Arge at AFRL and the ENLIL Model was developed by D. Odstrcil at GMU.

REFERENCES

Acuña, M. H., Curtis, D., Scheifele, J. L., et al. 2008, SSRv, 136, 203
Arge, C. N., Luhmann, J. G., Odstrcil, D., Schrijver, C. J., & Li, Y. 2004, JASTP, 66, 1295
Arge, C. N., & Pizzo, V. J. 2000, JGR, 105, 10465
Bain, H. M., Krucker, S., Saint-Hilaire, P., & Raftery, C. L. 2014, ApJ, 782, 43
Baker, D. N., Li, X., Pulkkinen, A., et al. 2013, SpWea, 11, 585

Brueckner, G. E., Howard, R. A., Koomen, M. J., et al. 1995, SoPh, 162, 357
Cane, H. V., Reames, D. V., & von Rosenvinge, T. T. 1988, JGR, 93, 9555
Cane, H. V., Richardson, I. G., & von Rosenvinge, T. T. 2010, JGRA, 115, A08101
Cash, M. D., Biesecker, D. A., Millward, G., Arge, C. N., & Henney, C. J. 2013, in 2013 AGU Fall Meeting (San Francisco, CA: AGU), SH41B-2180
Domingo, V., Fleck, B., & Poland, A. I. 1995, SoPh, 162, 1
Galvin, A. B., Kistler, L. M., Popecki, M. A., et al. 2008, SSRv, 136, 437
Gopalswamy, N., Yashiro, S., Kaiser, M. L., Howard, R. A., & Bougeret, J.-L. 2001, ApJL, 548, L91
Gopalswamy, N., Yashiro, S., Michałek, G., et al. 2002, ApJL, 572, L103
Harrison, R. A., Davies, J. A., Möstl, C., et al. 2012, ApJ, 750, 45
Harvey, J. W., Hill, F., Hubbard, R. P., et al. 1996, Sci, 272, 1284
Howard, R. A., Moses, J. D., Vourlidas, A., et al. 2008, SSRv, 136, 67
Jian, L. K., MacNeice, P. J., Taktakishvili, A., et al. 2015, SpWea, 13, 316
Jian, L. K., Russell, C. T., Luhmann, J. G., et al. 2011, SoPh, 273, 179
Jian, L. K., Russell, C. T., Luhmann, J. G., Galvin, A. B., & Simunac, K. D. C. 2013, in AIP Conf. Ser. 1539 (Melville, NY: AIP), 191
Kahler, S. W. 2001, JGR, 106, 20947
Kaiser, M. L., Kucera, T. A., Davila, J. M., et al. 2008, SSRv, 136, 5
Kallenrode, M.-B., & Wibberenz, G. 1997, JGR, 102, 22311
Lario, D., Aran, A., Gómez-Herrero, R., et al. 2013, ApJ, 767, 41
Lario, D., Sanahuja, B., & Heras, A. M. 1998, ApJ, 509, 415
Lee, C. O., Arge, C. N., Odstrčil, D., et al. 2013, SoPh, 285, 349
Leske, R. A., Cohen, C. M. S., Dotson, B., et al. 2013, in AIP Conf. Ser. 1539, SOLAR WIND 13: Proceedings of the Thirteenth International Solar Wind Conference (Melville, NY: AIP), 227
Leske, R. A., Cohen, C. M. S., Mewaldt, R. A., et al. 2012, SoPh, 281, 301
Leske, R. A., Cummings, A. C., Cohen, C. M. S., et al. 2014, in ASP Conf. Ser. 484, Outstanding Problems in Heliophysics: From Coronal Heating to the Edge of the Heliosphere, ed. Q. Hu & G. P. Zank (San Francisco, CA: ASP), 117
Liu, Y. D., Luhmann, J. G., Kajdič, P., et al. 2014, NatCo, 5, 3481
Liu, Y. D., Luhmann, J. G., Möstl, C., et al. 2012, ApJL, 746, L15
Lugaz, N., Farrugia, C. J., Smith, C. W., & Paulson, K. 2015, JGRA, 120, 2409
Luhmann, J. G., Curtis, D. W., Schroeder, P., et al. 2008, SSRv, 136, 117
Luhmann, J. G., Ledvina, S. A., Odstrcil, D., et al. 2010, AdSpR, 46, 1
MacNeice, P. 2009, SpWea, 7, S12002
MacNeice, P., Elliott, B., & Acebal, A. 2011, SpWea, 9, S10003
Martínez Oliveros, J. C., Raftery, C. L., Bain, H. M., et al. 2012, ApJ, 748, 66
Mays, M. L., Taktakishvili, A., Pulkkinen, A., et al. 2015, SoPh, 290, 1775
McComas, D. J., Bame, S. J., Barker, P., et al. 1998, SSRv, 86, 563
Mewaldt, R. A., Cohen, C. M. S., Cook, W. R., et al. 2008, SSRv, 136, 285
Millward, G., Biesecker, D., Pizzo, V., & Koning, C. A. 2013, SpWea, 11, 57
Möstl, C., Farrugia, C. J., Kilpua, E. K. J., et al. 2012, ApJ, 758, 10
Ngwira, C. M., Pulkkinen, A., Leila Mays, M., et al. 2013, SpWea, 11, 671
Odstrcil, D. 2003, AdSpR, 32, 497
Odstrcil, D., Riley, P., & Zhao, X. P. 2004, JGRA, 109, A02116
Odstrčil, D., Smith, Z., & Dryer, M. 1996, GeoRL, 23, 2521
Reames, D. V. 1999, SSRv, 90, 413
Richardson, I. G. 1994, ApJ, 420, 926
Richardson, I. G., & Cane, H. V. 2010, JGRA, 115, A07103
Richardson, I. G., & Reames, D. V. 1993, ApJS, 85, 411
Russell, C. T., Mewaldt, R. A., Luhmann, J. G., et al. 2013, ApJ, 770, 38
Schrijver, C. J., & Title, A. M. 2011, JGRA, 116, 4108
Smith, C. W., L'Heureux, J., Ness, N. F., et al. 1998, SSRv, 86, 613
Steed, K., & Lapenta, G. 2011, in 2011 AGU Fall Meeting (San Francisco, CA: AGU), SH23C-1974
Stone, E. C., Frandsen, A. M., Mewaldt, R. A., et al. 1998, SSRv, 86, 1
Taktakishvili, A., MacNeice, P., & Odstrcil, D. 2010, SpWea, 8, S06007
Temmer, M., & Nitta, N. V. 2015, SoPh, 290, 919
Temmer, M., Vršnak, B., Rollett, T., et al. 2012, ApJ, 749, 57
Thernisien, A., Vourlidas, A., & Howard, R. A. 2009, SoPh, 256, 111
von Rosenvinge, T. T., Reames, D. V., Baker, R., et al. 2008, SSRv, 136, 391